Faculteit Industriële Ingenieurswetenschappen

master in de industriële wetenschappen: nucleaire technologie

Masterthesis

Whole-body dMRI With EPI Distortion Correction: A Prospective Cross-sectional Observational Study

Jeremy Madhvani

Scriptie ingediend tot het behalen van de graad van master in de industriële wetenschappen: nucleaire technologie, afstudeerrichting nucleair en medisch

PROMOTOR :
Prof. dr. Brigitte RENIERS

PROMOTOR :
Prof. dr. Vincent VANDECAVEYE

COPROMOTOR :
Dr. Ahmed RADWAN

Gezamenlijke opleiding UHasselt en KU Leuven

Universiteit Hasselt | Campus Diepenbeek | Faculteit Industriële Ingenieurswetenschappen | Agoralaan Gebouw H - Gebouw B | BE 3590 Diepenbeek

Universiteit Hasselt | Campus Diepenbeek | Agoralaan Gebouw D | BE 3590 Diepenbeek
Universiteit Hasselt | Campus Hasselt | Martelarenlaan 42 | BE 3500 Hasselt

2023
2024

Faculteit Industriële Ingenieurswetenschappen

master in de industriële wetenschappen: nucleaire technologie

Masterthesis

Whole-body dMRI With EPI Distortion Correction: A Prospective Cross-sectional Observational Study

Jeremy Madhvani

Scriptie ingediend tot het behalen van de graad van master in de industriële wetenschappen: nucleaire technologie, afstudeerrichting nucleair en medisch

PROMOTOR :

Prof. dr. Brigitte RENIERS

PROMOTOR :

Prof. dr. Vincent VANDECAVEYE

COPROMOTOR :

Dr. Ahmed RADWAN

UHASSELT KU LEUVEN

Preface

The idea of this subject was provided by Prof. Vincent Vandecaveye and Dr. Ahmed Radwan, I would like to thank them both for allowing me to start this topic and for guiding me. I would also like to thank Prof. Hilde Bosmans for introducing me to Prof. Vandecaveye and his team, otherwise I would have never been able to start this thesis. I would also like to thank Prof. Brigitte Reniers for being my supervisor at the university, and for guiding me through this project. This thesis is very much in line with my daily work at the MRI department of a hospital, which is why I chose this specific topic. Non-research oriented MRI in practice tends to lose touch with the underlying theoretical aspects, and especially an advanced topic such as diffusion weighted imaging for the whole-body is not really elaborated on. I wanted to finish my Master's degree with a topic that I had worked with in practice, and this topic was perfect. This thesis allowed me to gain a better understanding of whole-body diffusion weighted imaging, image processing, and how imaging studies are carried out in practice. I combined these Master's studies with a job, which was definitely not easy, and the distance from school to home was very large. Luckily I have a beautiful 2 year old daughter who has really helped a lot in terms of dedication to succeed in these studies, thank you Noor. I would really like to give a special thank you to my wife Anne for her unconditional support and belief in me during these studies, thank you very much.

Table of contents

List of tables

List of figures

List of abbreviations and symbols

Abbreviation	Definition
TA	Acquisition time
ADC	Apparent diffusion coefficient
ASSD	Average symmetric surface distance
BUBD	Blip-up blip-down
CS	Compressed sense
DSI	Dice similarity index
DC	Distortion correction
dMRI	Diffusion magnetic resonance imaging
DWI	Diffusion weighted imaging
EPI	Echo planar imaging
FSE	Fast spin echo
FOV	Field of view
FE	Frequency encoding
TI	Inversion time
MRI	Magnetic resonance imaging
MAD	Mean absolute difference
MB	Multi-band sense
MM	Multiple myeloma
MI	Mutual information
MY-RADS	Myeloma Response Assessment and Diagnosis System
NSA	Number of signal averages
PI	Parallel imaging
PE	Phase encoding
PET	Positron emission tomography
PCa	Prostate cancer
RF	Radio frequency
ROI	Region of interest
RVD	Relative volume difference
RPG	Reverse polarity gradient
STIR	Short tau inversion recovery
SNR	Signal-to-noise ratio
SS-EPI	Single-shot echo planar imaging
SE	Slice encoding
SPAIR	Spectral adiabatic inversion recovery
SD	Standard deviation
TR	Repetition time
TE	Echo time
WBDWI	Whole-body diffusion weighted imaging
WBMRI	Whole-body magnetic resonance imaging

Symbol	Definition
ω_L	Angular Larmor frequencies
δ	Duration of gradient
γ	Gyromagnetic ratio
F_L	Larmor frequencies
G	Magnitude of gradient

Abstract

Whole-body diffusion weighted imaging (WBDWI) is widely performed in clinical practice but suffers from geometric distortions due to single-shot echo planar imaging (SS-EPI) acquisition techniques. An inline SS-EPI distortion correction method called EPIC is available for brain scans, but not for WBDWI. Therefore, this thesis investigates EPIC in the context of WBDWI.

First, a dedicated imaging protocol is created with EPIC implemented. Secondly, three healthy volunteers are scanned. Third, corrected and uncorrected imaging data is evaluated and compared quantitatively in terms of the following characteristics: apparent diffusion coefficient (ADC) values, signal-to-noise ratio (SNR), position of the spinal cord, inter-station alignment, and similarity. After and during the evaluation of imaging data, the protocol is optimized.

The maximum difference in ADC values is less than 4.5%. SNR improvements and reductions are measured of up to 58% and 13%, respectively. EPIC reduces distortion of the spinal cord by a mean value of 60% and improves inter-station alignment by an average of 51%. When EPIC is used, mutual information with respect to T2 images is on average 0.037 higher. In summary, EPIC does not significantly change the ADC values of tissues, but may increase or decrease the SNR. Inter-station alignment, spinal cord distortion, and structure similarity are improved by applying EPIC. A dedicated whole-body protocol with EPIC is made, which can be further used for testing on a clinical patient population.

Abstract (Dutch)

Whole-body diffusion weighted imaging (WBDWI) wordt vaak uitgevoerd, maar is onderhevig aan vervormingen door het gebruik van *single-shot echo planar imaging* (SS-EPI)-acquisitietechnieken. Een *inline* SS-EPI-correctiemethode (EPIC) is beschikbaar voor hersenscans, maar niet voor WBDWI. Deze masterproef onderzoekt EPIC in de context van WBDWI.

Eerst wordt een aangepast scanprotocol gemaakt met EPIC. Ten tweede worden drie gezonde vrijwilligers gescand. Ten derde worden de beelden van gezonde vrijwilligers kwantitatief geëvalueerd en vergeleken op basis van de volgende kenmerken: *apparent diffusion coëfficiënt* (ADC)-waarden, signaal-ruisverhouding (SNR), positie van het ruggenmerg, *inter-station* uitlijning, en similariteit. Na en tijdens de evaluatie van de beelden wordt het protocol geoptimaliseerd.

Het maximale verschil in ADC-waarden is kleiner dan 4,5%. SNR-stijgingen en dalingen tot respectievelijk 58% en 13% zijn gemeten. EPIC vermindert de vervorming van het spinale kanaal met gemiddeld 60% en verbetert de uitlijning tussen stations met gemiddeld 51%. *Mutual information* van gecorrigeerde beelden is gemiddeld 0,037 hoger dan bij ongecorrigeerde beelden, ten aanzien van T2-beelden. De conclusie is dat EPIC de ADC-waarden van weefsels niet noemenswaardig verandert maar de SNR kan verhogen of verlagen. De uitlijning tussen stations, spinaalkanaalvervorming, en similariteit verbeteren door EPIC. Een gericht *whole-body* scanprotocol met EPIC is gemaakt, dat verder gebruikt kan worden om te testen op een klinische populatie.

1 Introduction

Diffusion weighted imaging (DWI) is a magnetic resonance imaging (MRI) technique which is based on the differences in Brownian motion of molecules. To measure diffusion using MRI, a standard pulse sequence is adapted to include the application of a linear gradient. The gradient induces a phase change in the nuclei which is then cancelled by a second gradient pulse if particles remain stationary. Stationary nuclei indicate restricted diffusion in tissue which may correspond to certain pathologies and allows differentiation between them. A value called "b" is an important parameter in DWI and is proportional to the square of the gradient strength [1]. In clinical practice, DWI is performed during the majority of examinations. Diffusion sequences can be added to examinations of specific body parts (e.g. brain), or whole-body diffusion weighted imaging (WBDWI) can be performed [2].

WBDWI is typically performed using single-shot echo-planar imaging (SS-EPI) acquisition techniques, which allow fast acquisition times [3]. In SS-EPI, the k-space is filled in one repetition time (TR). This is accomplished by rapid readout and phase gradient switching. The polarity of the readout gradient is rapidly switched, which is referred to as oscillating. The phase gradient is not oscillating but its amplitude is decreased every echo, which is called blipping [4].

WBDWI is currently being used to diagnose and follow-up a variety of diseases. Generally, WBDWI is combined with morphological T1 and T2 whole body sequences to provide a full examination. An important application is the use of WBDWI in combination with anatomical whole-body magnetic resonance imaging (WBMRI) for the initial staging of breast cancer. A recent study [5] has shown the aptitude of routine WBDWI as a surrogate to positron emission tomography (PET) for the initial staging of breast cancer, where WBDWI has proven to be superior in detecting bone metastases. Another important indication is multiple myeloma (MM), where "Myeloma Response Assessment and Diagnosis System" (MY-RADS) guidelines have been established for the acquisition, interpretation, and reporting of WBMRI in MM [6]. The MY-RADS protocol has been qualitatively and quantitatively tested in terms of image quality and has proven to deliver good image quality [7]. Other indications for using WBDWI combined with anatomical WBMRI are prostate cancer (PCa), melanoma, ovarian cancer, lymphoma, lung cancer, colorectal cancer, and cancer screening [8]. The advantage of using WBDWI to monitor treatment response is found in its ability to determine the state of an osseous lesion, which is not possible with conventional imaging techniques [9]. Given the advantages regarding osseous lesions, WBDWI is also widely used for the detection of bone metastasis in PCa patients [10].

WBDWI is widely performed in clinical practice but still suffers from imaging artifacts, mainly as a result of the use of SS-EPI. Artifacts diminish image quality and can obscure areas prone to geometric distortions, such as tissue boundaries [11]. The main artifacts arising are geometric warping from magnetic field inhomogeneities, geometric warping from gradient-induced eddy currents, and intra-voxel dephasing effects.
Magnetic field inhomogeneities generally arise from tissue/air boundaries and are especially disturbing around metal. Also, as soon as any object enters the MRI machine, the magnetic field is disturbed. The change in magnetic field causes a change in resonance frequency of the spins. This changed frequency is called an off-resonance frequency and induces geometric shifting, or warping of the image. Typical inhomogeneities are in the order of 100 Hz and with frequency encoding gradient strengths of 500-1000 Hz/mm, this poses no meaningful issues. On the other hand, the phase encoding gradient strength is smaller ($\approx$ 10 Hz/mm) because of the limited 2π phase interval it can distribute amongst its axis [12].

Eddy currents can also give rise to geometric warping of the final image. These effects are created by the long diffusion gradients and can be reduced by using parallel imaging (PI) techniques because this encodes the y-direction of k-space much faster. The eddy current effects are less pronounced than field inhomogeneities in modern scanners because of hardware and software upgrades.
Dephasing artifacts are caused by the dephasing of the spins during the sampling and give rise to signal loss and a reduction of the resolution because high spatial frequencies are collected near the end of sampling. Dephasing artifacts increase with increased readout duration. Again, a useful method for reducing this effect is PI which effectively reduces the sampling duration [13]. These artifacts are also called blurring artifacts and increase in magnitude with increasing B_0 field strength due to very short dephasing times. Generally blurring artifacts are insignificant compared to geometric distortion artifacts but do become important at field strengths of 7 T [14].

To conclude, the leading dominant artifact in SS-EPI is spatial distortion and because WBDWI is typically performed using this technique, correcting for this distortion is necessary. An inline EPI distortion correction method by Philips (EPIC) is currently available for brain scans, but not for WBDWI. Therefore, this thesis will attempt to close this gap by exploring EPIC for whole-body scans. The first research question of this study is whether the standard diffusion sequences can be modified to include EPIC for WBDWI purposes. Secondly, the adjusted sequence will be tested on healthy volunteers. Third, the performance of EPIC is quantitatively investigated, how does it perform when compared to non-EPIC scans? The first chapter (2) of this thesis serves as a brief introduction to magnetic resonance imaging (MRI) and DWI by means of a literature study. The second chapter (3) elaborates on the practical study, which includes materials, methods, results, and discussion. The last chapter (4) provides the conclusion and future outlook.

2 Literature study

This literature study investigates the principle of diffusion weighted imaging (DWI) in whole-body diffusion weighted imaging (WBDWI), and elaborates on the main imaging artifacts that arise from the DWI technique. The most important methods of artifact reduction and image quality assessment are also discussed. In the first chapter, a brief introduction to magnetic resonance imaging (MRI) and DWI is given. The second chapter explains the main imaging artifacts arising in DWI, and their sources. Finally, the third chapter discusses methods to resolve imaging artifacts, and reviews image quality assessment methods.

2.1 Principle of MRI and DWI

This chapter offers a brief introduction to the basics of MRI and diffusion magnetic resonance imaging (dMRI).

2.1.1 Conventional imaging

Imaging starts with the emission of a 90° radio frequency (RF) pulse with a certain bandwidth, which is called the excitation pulse. The excitation pulse is repeated each repetition time (TR). The frequency of the excitation pulse is based on the Larmor frequencies (F_L) of the nuclei and these frequencies are defined by the Larmor equation:

$$F_L = \gamma B \tag{1}$$

The gyromagnetic ratio γ is specific for the studied nucleus, which is typically hydrogen ($\gamma_{hydrogen}$ = 42.58 MHz/T). To select specific nuclei, the magnetic field strength (B) in equation 1 is altered due to gradients in the scanner. After the excitation pulse, the selected nuclei become less aligned with the main magnetic field (longitudinal) and the transversal magnetization increases. Immediately after the excitation, the nuclei lose transverse magnetization due to magnetic field inhomogeneities and interactions with neighboring nuclei. To restore the transverse magnetization, a 180° RF pulse is applied a time τ after the excitation pulse. The signal then appears after 2τ when phases align. The basic principle is shown in Fig. 1 [1].

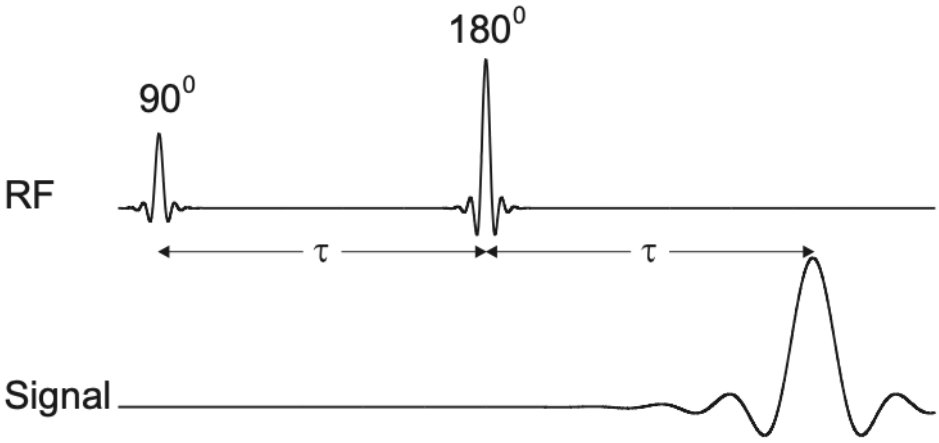

Fig. 1. Basic principle of generating a MRI signal [1, p. 5]

Transverse magnetization is measurable as phase and frequency information, which is then registered in a matrix called the k-space. During image formation, the k-space is filled with phase- and frequency encoded data corresponding to the frequency domain of the spatial representation of the image (Fig. 2). In order to generate a complete image, the k-space must be filled completely. After the k-space is filled, the spatial representation can be obtained by using the inverse Fourier transform on the k-space [4].

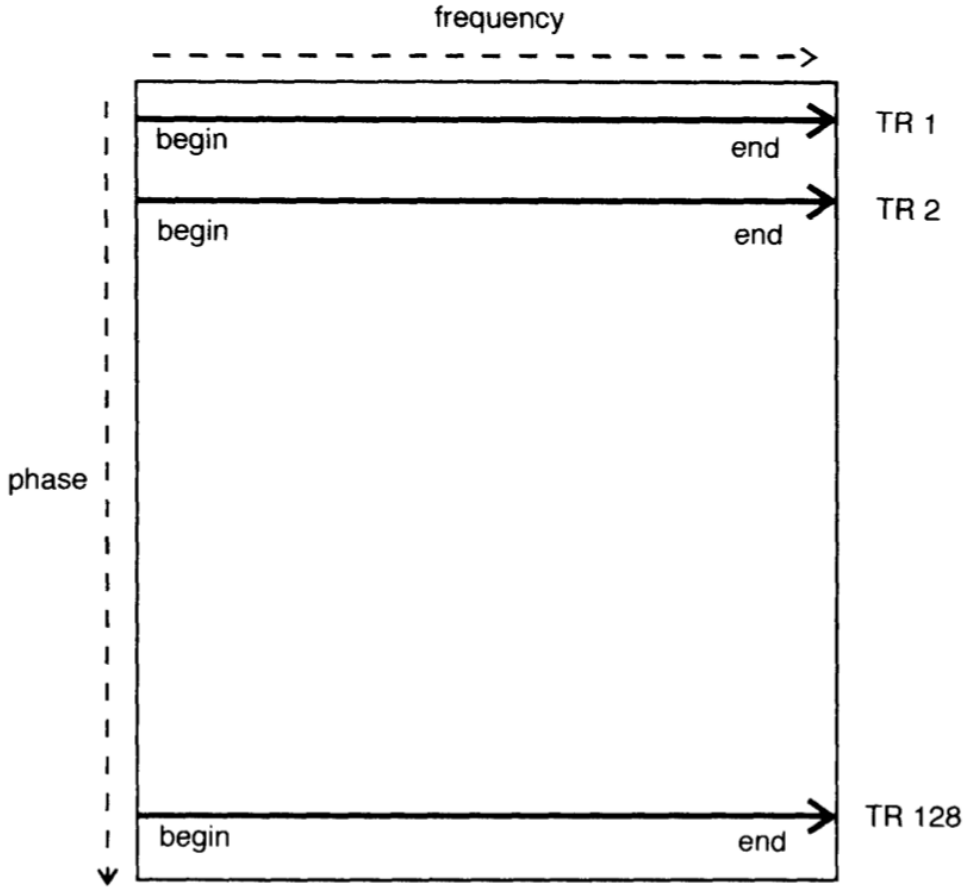

Fig. 2. Conventional filling of the k-space [2, p. 133]

2.1.2 Diffusion weighted imaging

DWI is a technique used in MRI which is based on the differences in Brownian motion of molecules. To measure diffusion using MRI, the standard pulse sequence shown in Fig. 1 is adapted to include the application of a gradient pulse (Fig. 3).

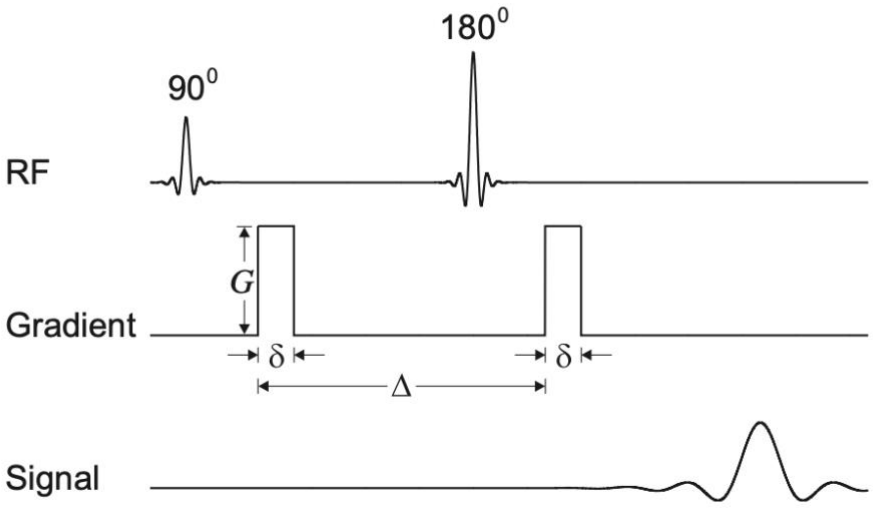

Fig. 3. Principle of a diffusion sequence [1, p. 6]

In Fig. 3, "G" and "δ" are the magnitude and the duration of the gradient, respectively. The gradients in Fig. 3 are assumed linear, and the magnitude of the additionally applied magnetic field is dependent of the position x. As shown in Fig. 4, the actual gradients are not linear but do approach linearity in proximity of the imaging field of view (FOV) [13].

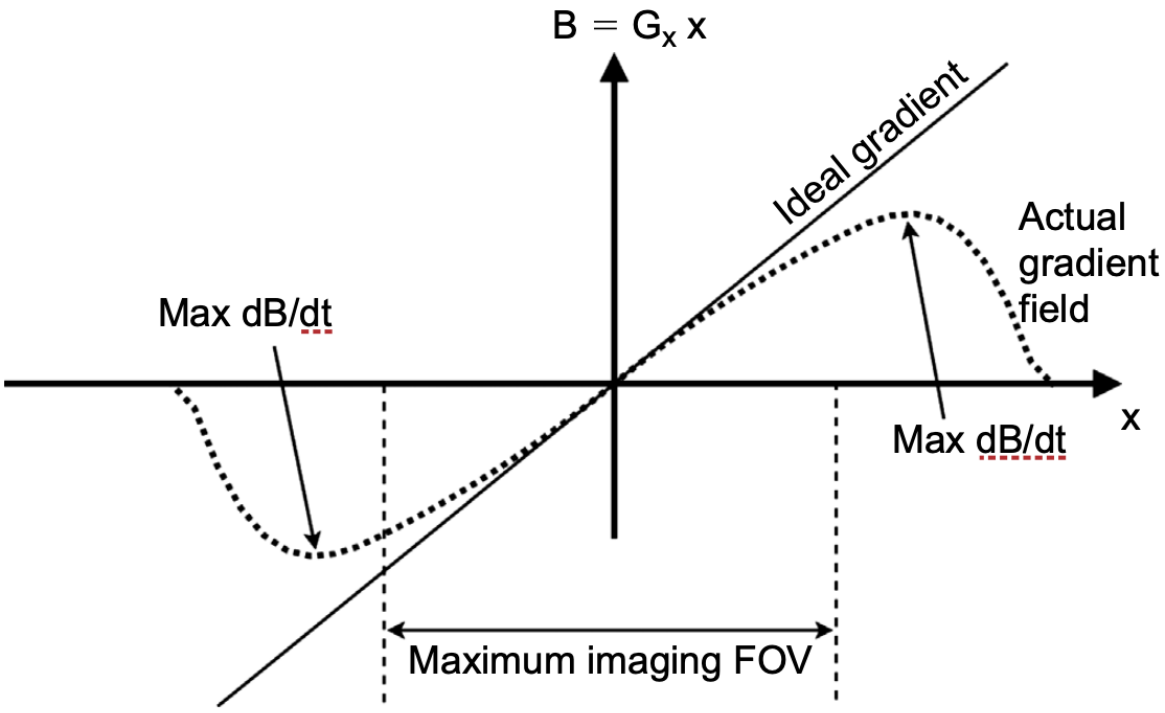

Fig. 4. Non-linearity of gradients used in DWI [3, p. 21]

Fig. 3 and 4 show that a particle will experience a change in magnetic field of $G(x)\delta$, which – when multiplied by the gyromagnetic ratio and 2π – will cause a phase change equal to $2\pi\gamma\delta G(x)$. When dealing with phases, the Larmor frequencies are often described as angular Larmor frequencies (ω_L), this is equation 1 multiplied by 2π. A particle situated at position x_0 during the first gradient pulse will acquire a phase change of $2\pi\gamma\delta G(x_0)$. After the first gradient pulse, a 180° refocusing RF pulse is applied which effectively reverses the acquired phase change during the first gradient pulse. The net phase change of the particle after the 180° RF pulse is then

$$\theta_0 = -2\pi\gamma\delta G(x_0) \tag{2}$$

which is followed by another gradient pulse when the particle diffused from x_0 to x_1 resulting in a total phase change of

$$\theta_T = 2\pi\gamma\delta(G(x_1) - G(x_0)) \tag{3}$$

Equation 3 shows that when a particle remains stationary ($x_0 = x_1$), the net phase change is zero and it will not acquire any phase change. Thus, if particles remain stationary the generated signal will be high and show up as bright on the image. Stationary nuclei indicate restricted diffusion in tissue which may correspond to certain pathologies and allows a differentiation to be made between them. A value called "b" is an important parameter in DWI and is proportional to the square of the gradient strength. It is important to note that in some tissue types diffusion is independent of diffusion direction (grey matter), while in others it is dependent of the chosen gradient direction (white matter), thus in some cases a single direction is insufficient for defining the diffusion in tissue, but the basic principle remains the same [1].

2.1.3 Applications of DWI

In clinical practice DWI is performed during the majority of exams. One application of DWI is found in the field of oncology. In onco-imaging a diffusion sequence can be added to the exam to provide additional information about a specific region of interest (e.g. brain), or WBDWI can be performed [2]. Generally WBDWI is combined with morphological T1 and T2 whole body sequences to provide a full examination. WBDWI is currently being used to diagnose and follow-up a variety of diseases. One example is the use of WBDWI in combination with anatomical whole-body MRI (WBMRI) for the initial staging of breast cancer. A recent study [5] has shown the aptitude of routine WBDWI as a surrogate to PET-CT for the initial staging of breast cancer, where WBDWI has proven to be superior in detecting bone metastases. Another important indication is multiple myeloma, where Myeloma Response Assessment and Diagnosis System (MY-RADS) guidelines have been established for the acquisition, interpretation, and reporting of WBMRI in multiple myeloma [6]. The MY-RADS protocol has been qualitatively and quantitatively tested in terms of image quality and has proven to deliver good image quality [7]. Other indications for using WBDWI combined with anatomical WBMRI are prostate cancer (PCa), melanoma, ovarian cancer, lymphoma, lung cancer, colorectal cancer, and cancer screening [8]. The advantage of using WBDWI to monitor treatment response is found in its ability to determine the state of an osseous lesion, which is not possible with conventional imaging techniques [9]. Given the advantages regarding osseous lesions, WBDWI is also widely used for the detection of bone metastasis in PCa patients [10].

2.1.4 Echo planar imaging

Whole-body diffusion scans are typically performed using single-shot echo-planar imaging (SS-EPI) acquisition techniques, which allow fast acquisition times [3]. SS-EPI is a type of acquisition method where all k-space lines are filled during one TR. The k-space contains the spatial frequency information necessary to form the image. Finishing an acquisition requires filling all k-space lines which means rapid readout and phase gradient switching is necessary (Fig. 5). The polarity of the readout gradient is also rapidly switched which is called oscillating. The phase gradient is not oscillating but its amplitude is decreased every echo, which is called blipping. SS-EPI can be described as filling the k-space without lifting the pen from the paper while conventional acquisition techniques use multiple TRs. Because echo planar imaging (EPI) is such a fast technique, whole body scans can theoretically be done in 30 seconds. That being said, the image quality of such fast scans is poor. In order to improve image quality, k-space segmentation can be implemented. In k-space segmentation the k-space is filled in multiple times [4]. Alternatively, multiple measurements can be performed instead of one. Both methods improve image quality but increase the acquisition time, which is unwanted in whole-body imaging. This calls for other methods of artifact reduction.

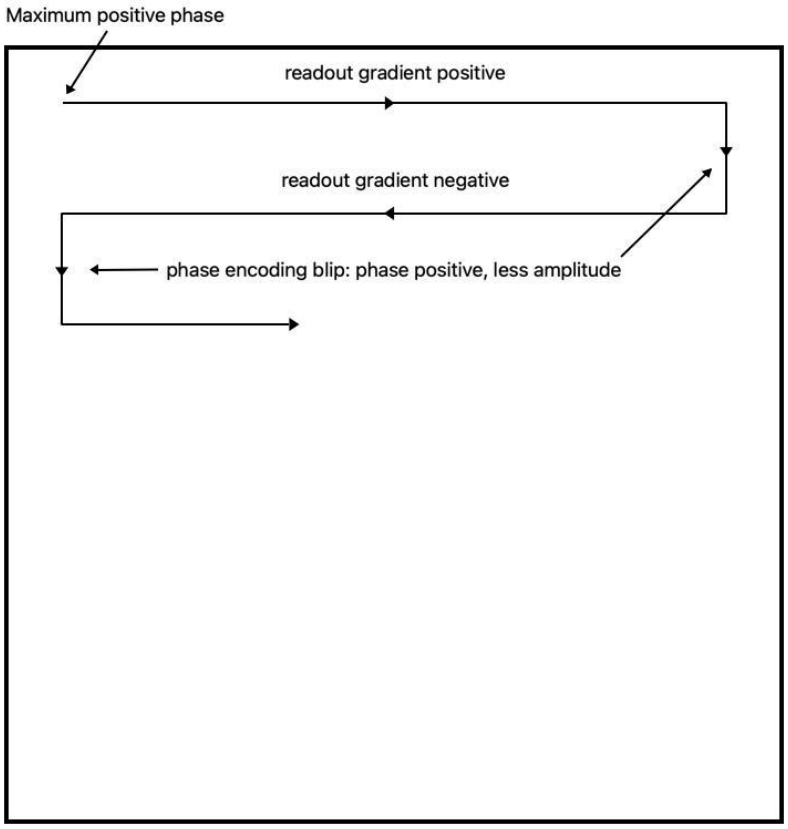

Fig. 5. Rapid switching of gradients in EPI to fill the k-space in one TR [2, p. 133]

2.2 Nature of imaging artifacts

2.2.1 General DWI artifacts

In DWI, the gradients are responsible for two types of error producing mechanisms, i.e. eddy currents and gradient non-linearities. The magnetic fields produced by the gradient coils can give rise to eddy currents in nearby conductive surfaces, such as the cryostat (contains liquid helium) and RF coils. As a sequence requires the rapid switching of gradients, eddy currents can cause a delay in the change of these gradients. The eddy currents in surrounding conductive surfaces can induce magnetic fields which combine with the applied gradients. In this way the gradient encoding experienced by the spins is not the same as was programmed in order to produce and reconstruct the image. In other words this means that when the diffusion gradients are turned off, they actually persist for some time into the imaging gradients, creating image warping (i.e. geometric distortion). The eddy currents also change the actual shape of a voxel which leads to more inaccuracy. The effect of eddy currents on the resulting image can be summarized in three main artifacts: contraction, shifting, and shear (Fig. 6). The second problem with diffusion gradients is the non-linearity of the gradient. Due to conflicting requirements these gradients show non-linear behavior (Fig. 4). Because the gradients are not linear in the imaging volume, neither is the diffusion weighting, recall that the b-value is proportional to the square of the gradient strength [15].

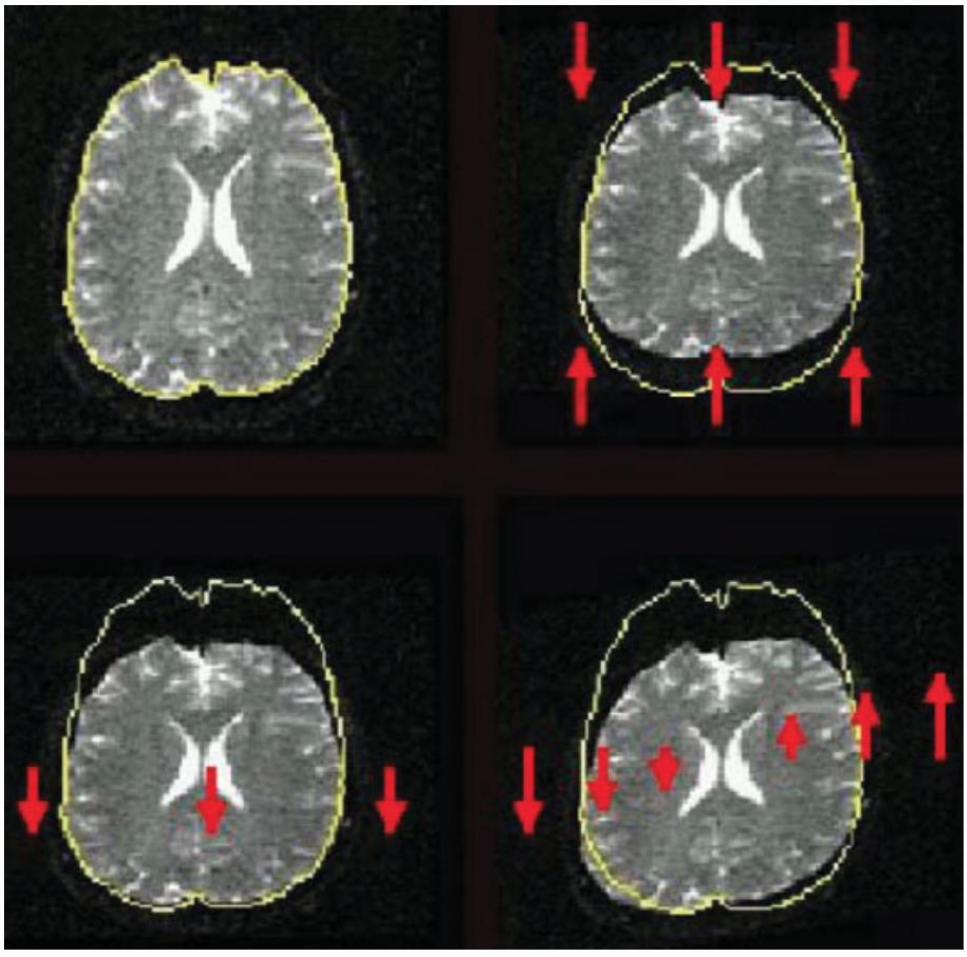

Fig. 6. Eddy current effect. Top-left: original, top-right: contraction, bottom-left: shifting, and bottom-right: shear [12, p. 481]

Currently, eddy current artifacts are primarily reduced due to hardware improvements. Actively shielded gradient coils have become standard in every modern MRI machine, the gradient coils are equipped with additional wiring to counter arising eddy currents [16]. As MRI hardware keeps improving over the years, limiting eddy current artifacts when performing WBMRI starts with the use of the latest hardware available.

2.2.2 Difficulties of EPI

In this thesis, SS-EPI acquisition techniques are used for imaging due to the fast nature of these sequences, considering the region of interest (ROI) is the whole-body of the patient, acquisition time is of great importance. Although SS-EPI sequences offer significant advantages compared to multi-shot methods, SS-EPI sequences also face several challenges related to image quality. These are geometric warping from magnetic field inhomogeneities, geometric warping from gradient-induced eddy currents, and intra-voxel dephasing effects. The reason EPI sequences are extremely sensitive to these artifacts is shown in Fig. 7 [12].

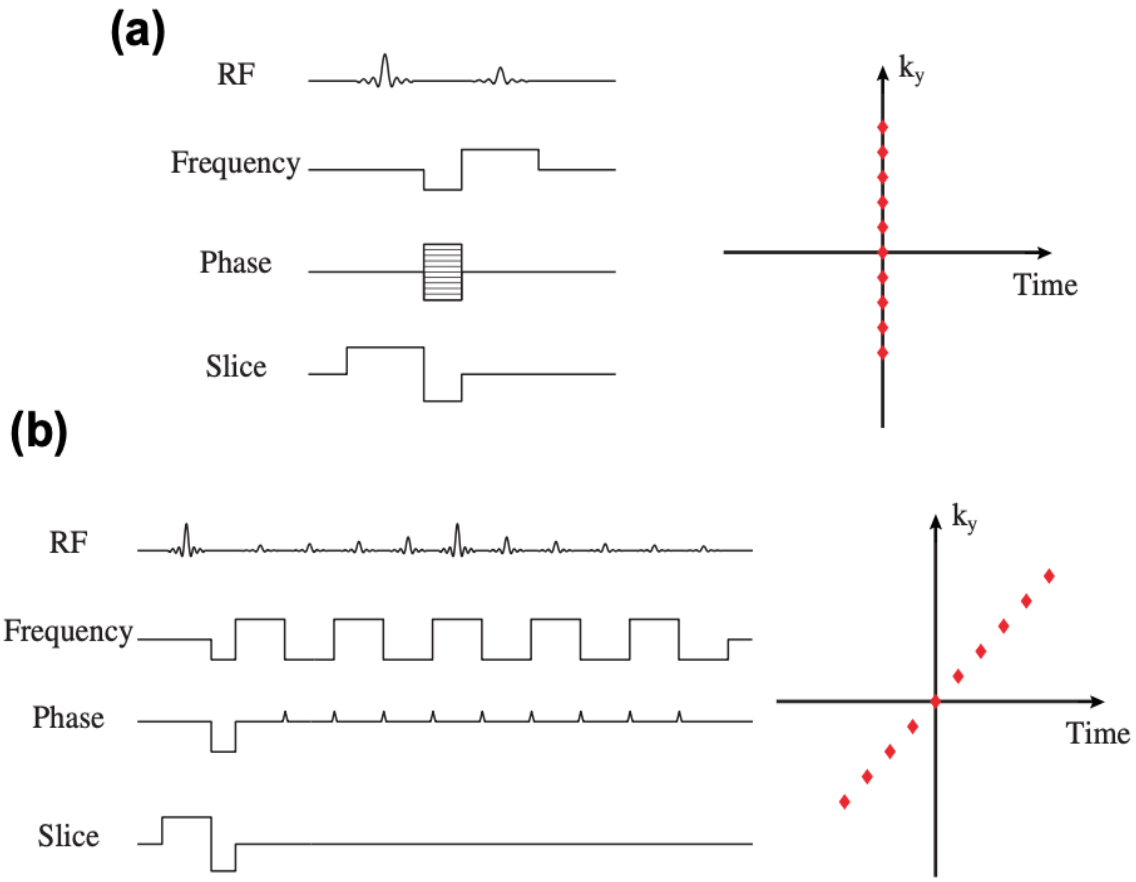

Fig. 7. Reason for EPI distortion sensitivity. (a) Non-EPI sequence. (b) EPI sequence [14, p. 65]

Fig. 7 shows a non-EPI sequence (a), and an EPI sequence (b). The non-EPI sequence resets the phase accumulation of distorted off-resonance voxels every TR. In the EPI sequence only one TR is used, so in other words, the phase accumulation of distorted off-resonance voxels is not cancelled. This phenomenon causes misplacement of off-resonance voxels into different areas where they actually do

not belong, leading to distortion of the resulting image. Magnetic field inhomogeneities generally arise from tissue/air boundaries and are especially disturbing around metal. Also, as soon as any object enters the MRI machine, the magnetic field is disturbed. In this study, the presence of metallic implants that may alter the magnetic field is an exclusion criteria for patient and volunteer selection. The change in magnetic field causes a change in resonance frequency of the spins as explained by altering equation 1 into equation 4:

$$\Delta f = \gamma \Delta B \tag{4}$$

This changed frequency is called an off-resonance frequency and induces geometric shifting, or warping of the image. As equation 4 shows, the off-resonance frequency is proportional to the field strength, so distortion effects increase with increasing field strength. This statement is also supported by the results of [17], where 1.5 T and 3 T scanners were compared in terms of geometric distortion. In this study, a static magnetic field strength of 3 T is used, to offer a greater signal-to-noise ratio (SNR), and thus reduce imaging time, which compensates for the increased off-resonance frequencies. The distortions occur in the phase encoding (PE) direction and are negligible in the frequency encoding (FE) direction. Typical inhomogeneities are in the order of 100 Hz and with FE gradient strengths of 500-1000 Hz/mm this poses no meaningful issues. On the other hand, the PE gradient strength is smaller (on average 10 Hz/mm) because of the limited 2π phase interval it can distribute amongst its axis [12]. How these field inhomogeneities affect image reconstruction is shown visually in Fig. 8.

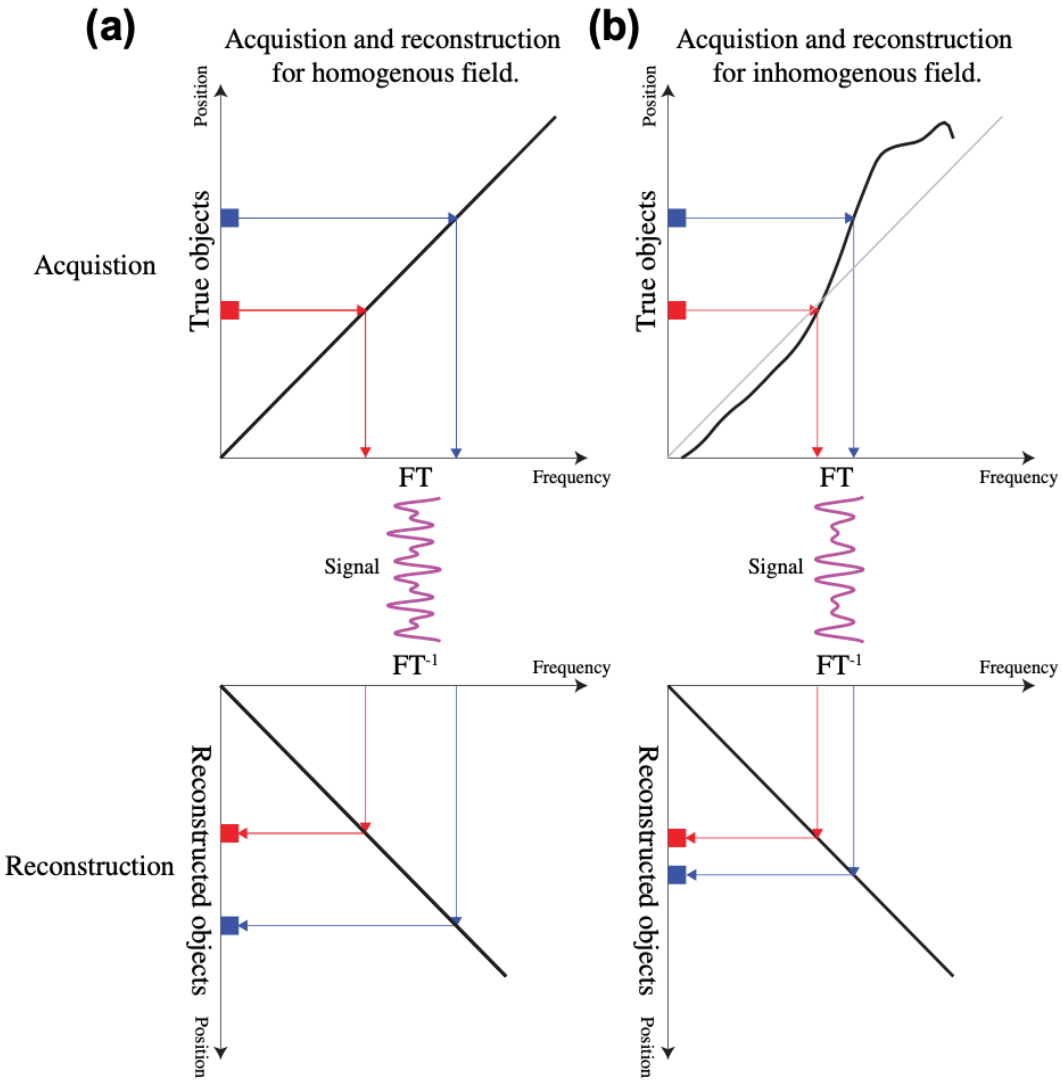

Fig. 8. How distortion in EPI sequences from field inhomogeneities arise. (a) The ideal case, no distortion appears in the reconstructed image. (b) The non-linear case where an off-resonance field causes distortion during image reconstruction. FT refers to the Fourier transform [14, p. 66]

Fig. 8a shows, that when there are no magnetic field inhomogeneities present, the resulting positions of the voxels are reconstructed correctly. On the other hand, when field inhomogeneities allow voxels to acquire phase changes as explained in equation 4, voxels are mapped to wrong positions (Fig. 8b). A visual representation of this phenomenon in brain imaging is shown in Fig. 9a.

Another group of artifacts is dephasing artifacts, these are caused by the dephasing of the spins during sampling and give rise to signal loss and a reduction of the resolution because high spatial frequencies are collected near the end of sampling. Dephasing artifacts increase with increased readout duration. A useful method for reducing this effect is PI which effectively reduces the sampling duration [13]. These artifacts are also called (T2*) blurring artifacts and increase in magnitude with increasing B_0 field strength due to very short dephasing times. Generally, blurring artifacts are insignificant compared to geometric distortion artifacts but do become important at field strengths of 7 T [14]. Since the scanners used in this thesis are 3 T, these artifacts are insignificant compared to the geometric distortion artifact.

2.3 Distortion correction methods

Now that the general DWI artifacts and EPI specific difficulties have been discussed, it is time to elaborate on the methods used to reduce these artifacts, specifically in examinations concerning the whole-body. A common distortion correction method for whole-body applications is the reverse polarity gradient (RPG) method. Another frequently used correction method is field mapping. Both methods can be combined into one single distortion correction method, and this combined method will be explained in the next section.

2.3.1 EPI Distortion Correction (EPIC)

In this thesis, an inline distortion correction method is used, named "EPIC", made available for whole-body MRI by Philips, specifically for this study. EPIC combines two well-known distortion correction methods: the RPG method and field mapping. Voxels are misplaced due to static B_0 magnetic field inhomogeneities from magnetic properties of objects in the static field, as described in previous sections. The field mapping method provides a correction for the misplacement problem. Field mapping is described in great detail by [18] and involves obtaining a pixel shift map from a field inhomogeneity map. When the pixel shift map is obtained, the misplacement of voxels can then be corrected for. The RPG method relies on the acquisition of a B_0 pre-scan with an EPI blip-up blip-down (BUBD) pair. The BUBD technique is a common method for correcting geometric distortions as a result of performing diffusion with an EPI acquisition technique [19]. Because the distortion is directionally dependent, it is possible to acquire two images with reversed PE direction, where equal but opposite warping will be present (i.e. a BUBD pair). It is simply the k-space trajectory in fig. 5 (blip-down), and its reverse (blip-up). From the BUBD pair an estimated distortion field can be constructed representing the off-resonance voxels. Subsequently, the field map can be used to correct for the distortions. An example of applying EPIC in brain imaging is shown in Fig. 9, where (a) shows the uncorrected image, and (b) the corrected image. The uncorrected image shows signal loss and pile up near the frontal lobe. In the corrected image the signal loss has been restored and less pile up at the frontal lobe is present.

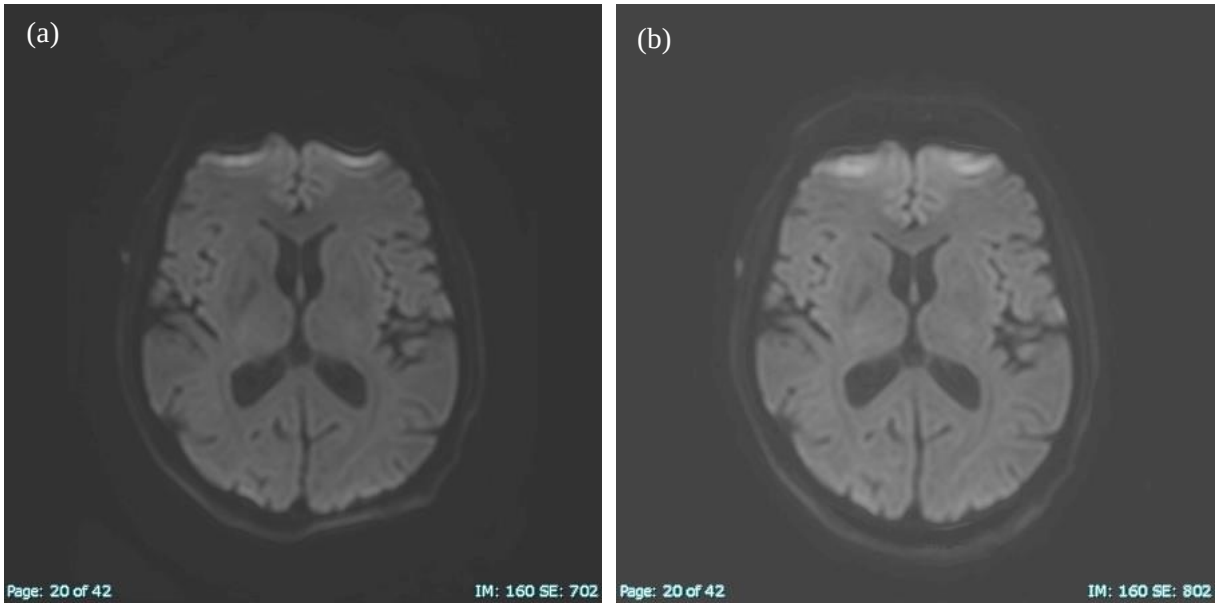

Fig. 9. Example of applying EPIC in brain imaging. (a) Uncorrected EPI diffusion image showing signs of distortion, signal loss and pile up near the frontal lobe. (b) Distortion corrected image using the RPG method by applying "EPIC"

Another useful addition is the use of PI techniques. PI reduces the number of PE steps needed to form the image, which influences the time interval where off resonance voxels can be assigned phases and thus reduces distortions [12]. An unwanted effect of PI is reduction of the SNR, where the reduction follows a √N relationship with N the reduction or acceleration factor. The MRI operator can control the SNR by changing the number of signal averages (NSA), which increases SNR with the same √N factor. In this way, a combination of PI and NSA offers a balance between SNR and acquisition time (TA). PI can be implemented in an EPI sequence with EPIC to offer a combined distortion reduction effect. If a desired SNR is defined, optimization is possible. The voxel size also has an effect on SNR, where larger voxels lead to a higher SNR. The maximum voxel size has to be defined, then a maximum acceleration factor through PI can be applied based on the desired SNR level. The size of a voxel depends on the FOV, acquisition matrix size, and slice thickness. Both the FOV and matrix size determine the in-plane resolution, or pixel size. It is important to note that a higher in-plane resolution (smaller pixel size) acquisition results in less severe distortion artifacts [20].

2.3.2 Distortion correction in practice

When looking at individual parts of the body, good results have been obtained using the RPG method [21], [22], [23], [24], [25]. However, these distortion correction results rely on post-processing tools, being mostly used by specialized centers. The need for an easy to apply distortion correction method is great, because for non-research oriented centers, a post-processing free option is missing. Four imaging stations/sections will be examined in this study: head/neck, thorax, abdomen, and pelvis.

The RPG method has been evaluated for the head/neck area by [21], the submandibular gland and spinal cord were selected as regions of interest (ROIs). Diffusion images were compared with distortion-free T2 weighted images using the following post-processing measurements: Dice Similarity Index (DSI), average symmetric surface distance (ASSD), relative volume difference (RVD), and distance between geometric centers. The distortion corrected images showed increased geometrical accuracy, thus proving the effectiveness of the RPG method in the head/neck area. An important observation during the same study is the suspected effect of swallowing by the patient during head/neck examinations, distortion correction proved to be ineffective in this case. Because artifacts due to patient movement are not correctable using the RPG method , it is advised to instruct the patient not to swallow during imaging in this area. The FOV for a dedicated head/neck examination is smaller than the FOV of a whole-body head/neck area because a single FOV must be chosen in whole-body examinations. The chosen whole-body FOV has to be large enough to include the largest imaged body part (e.g. abdomen or thorax).

In a study [22] regarding the effect of distortion correction by the RPG method in prostate examinations, the distortion corrected images were found to be able to improve quantitative apparent diffusion coefficient (ADC) analysis. The same study also found that when a higher amount of rectal gas is present, the amount of distortion is greater. An idea to reduce these unwanted gases is to administer a laxative before the examination. Although a laxative was not administered in that study, the patients received 1 mg intramuscular Glucagon® (Novo Nordisk, Bagsværd, Denmark) and 20 mg butylscopolamine bromide (Buscopan®, Boehringer-Ingelheim, Ingelheim, Germany) intravenously to suppress bowel movement and rectal gas build up. Another study [23] concerning prostate examinations proved that application of the RPG method improves tumor localization. However, in that particular study a specialized coil was used for prostate imaging; an endorectal coil. In whole-body studies multiple

coils are used, which are typically two anterior surface coils in combination with a posterior array receive coil.

Concerning the breast area, application of the RPG method provides increased cross-correlation between distortion corrected images and anatomical fast spin echo (FSE) images when compared to non-distortion corrected images [24]. It must be noted that, similar to the prostate studies, a dedicated breast coil was used in [24]. In [25], a dedicated endo-vaginal coil was used for cervix imaging, application of the RPG method resulted in improved correspondence with anatomical T2 weighted images.

The effect of applying the RPG method has thus been widely evaluated for separate body parts, mostly using dedicated coils, which is to be expected. An additional challenge for whole-body examinations is the inability to use dedicated coils and adjust the FOV. For abdominal imaging an intestine immobilizing agent should be administered to suppress bowel movement and rectal gas build up. When head/neck imaging is performed, the patient must be instructed to swallow as less as possible.

Whole-body examinations face additional challenges due to the size of the anatomy of interest. Because the ROI is much greater than the maximum FOV, whole-body scans are constructed in several parts corresponding to different sections of the body. These separate parts are obtained at several imaging stations. Once all imaging stations have been completed, all parts are combined into one image [26]. The main issues that arise from the separation of sections are inter-station intensity variations and inter-station misalignment. Concerning inter-station intensity variations, [27] developed a general correction method called intensity standardization, where a deformation field is constructed using a reference histogram and the current histogram. Three correction strategies for inter-station intensity standardization were later developed and tested by [28] on a clinical population with MM. The most successful method was direct registration, where no data from overlapping regions of different stations is used. Inter-station misalignment (Fig. 10) is another frequently occurring phenomenon in whole-body imaging, which also has to be corrected for.

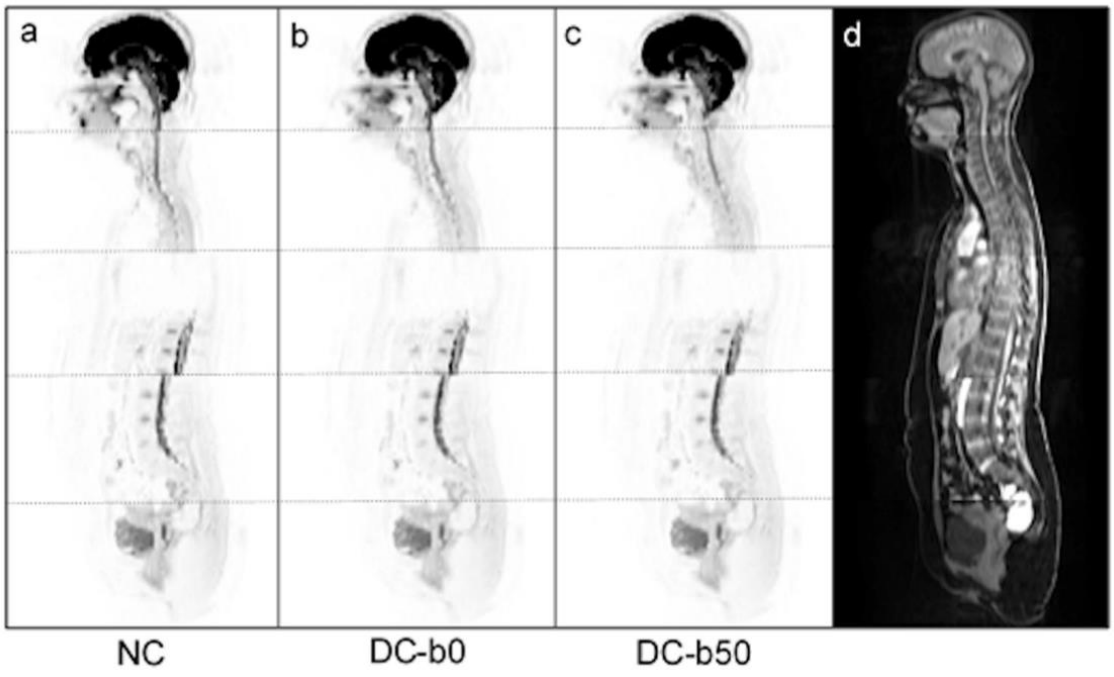

Fig. 10. Example of combining separate imaging stations into one image. Inter-station misalignments occur (a, b, c), which are less in the distortion corrected images (b, c) when compared to non-corrected images (a). (d) Structural image [15, p. 9]

Four registration methods were compared in [26] for correcting the inter-station misalignments. As explained in previous sections, diffusion images are very susceptible to different types of artifacts. Therefore, robust T1 weighted images were used as a reference for mapping the diffusion images. Four evaluation methods were used in [26].The first being the mean absolute difference (MAD), which is described by equation 5:

$$MAD = \frac{1}{k}\sum_{i=1}^{k}\frac{\sum_{x\in\Omega_i}|f(x)-g(x)|}{N_{\Omega_i}} \tag{5}$$

In equation 5, f(x) and g(x) are respectively the reference and transformed image intensities at neighboring ADC image stations in the overlapping region Ω_i. $N_{\Omega i}$ is the number of voxels in that overlapping region. The second image evaluation method consists of taking the partial derivative of the ADC image intensities along the z-direction over the region of overlap between stations, where large values would correspond to misalignment. An example is shown in Fig. 11, showing misalignment before and after correction. The third and fourth measurement performed in the study involved calculating the DSC of the spinal cord and between corresponding organs, respectively [26].

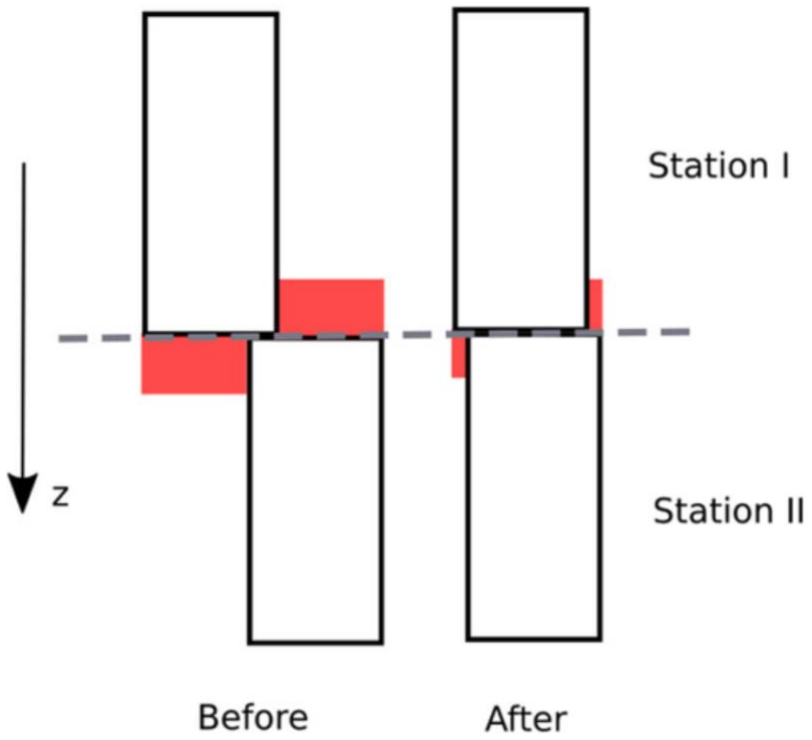

Fig. 11. Principle of an intensity edge map calculation [24, p. 1690]

2.3.3 Image quality assessment

To compare the image quality of non-distortion corrected images to distortion corrected images, several methods are available. This subsection explains the most widely used methods in WBDWI by using examples from distortion correction studies, both qualitative and quantitative methods are discussed.

A recent study [29] used anatomic landmarks to determine the performance of the reverse polarity method in whole-body studies. Fig. 12A shows a highlighted yellow line following the posterior edge of the vertebral column on T2 weighted images. The non-distortion corrected images (Fig. 12B) and distortion corrected images (Fig. 12C) show the same yellow line and in addition, a purple line tracing the same posterior edge of the vertebral column. This allows an accurate measurement of the error relative to the standard T2 weighted images, in terms of Euclidian distance between delineations. As already visible on Fig. 12, the distortion corrected images show less error when compared to non-distortion corrected variants. Another frequently used method is the similarity method, where structural images are compared to diffusion images in terms of their similarity. Two recent studies, [29] and [17], used this quality assessment method and found that the mutual information (MI) between diffusion weighted images and structural T2 weighted images significantly improved when distortion correction is applied (RPG method). Equation 6 is the DSC, which is often used as a measure of similarity between binary objects:

$$DSC = \frac{2|A \cap B|}{|A| + |B|} \tag{6}$$

In equation 6, $|A|$ and $|B|$ are the number of elements in the subsets. When both subsets are the same, the DSC is equal to 1 [26].

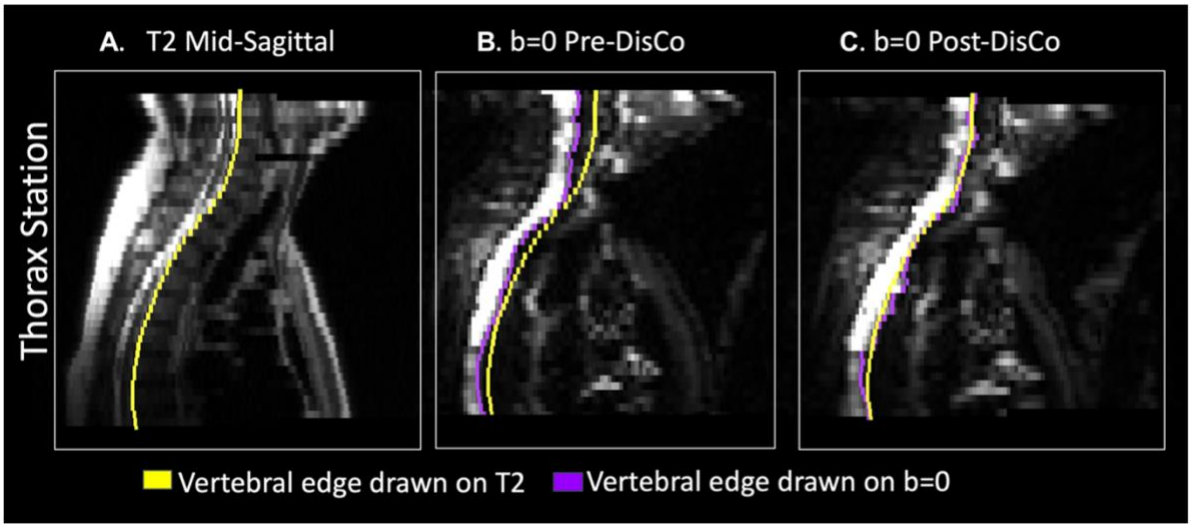

Fig. 12. Image quality assessment technique. Anatomic landmarks were used as a measure for the performance of distortion correction. (A) Standard T2 weighted reference image with the posterior edge of the vertebral column highlighted in yellow. Diffusion weighted image before distortion correction (B) and after (C). The purple line on B and C indicates the trace of the posterior vertebral column [27, p. 3]

Another quantitative method used in [29] is the assessment of bone metastasis displacement. By comparing a known bone metastasis based on T2 weighted structural images, the amount of distortion can be quantified, an example is shown in Fig. 13. The DSC can also be applied for this purpose.

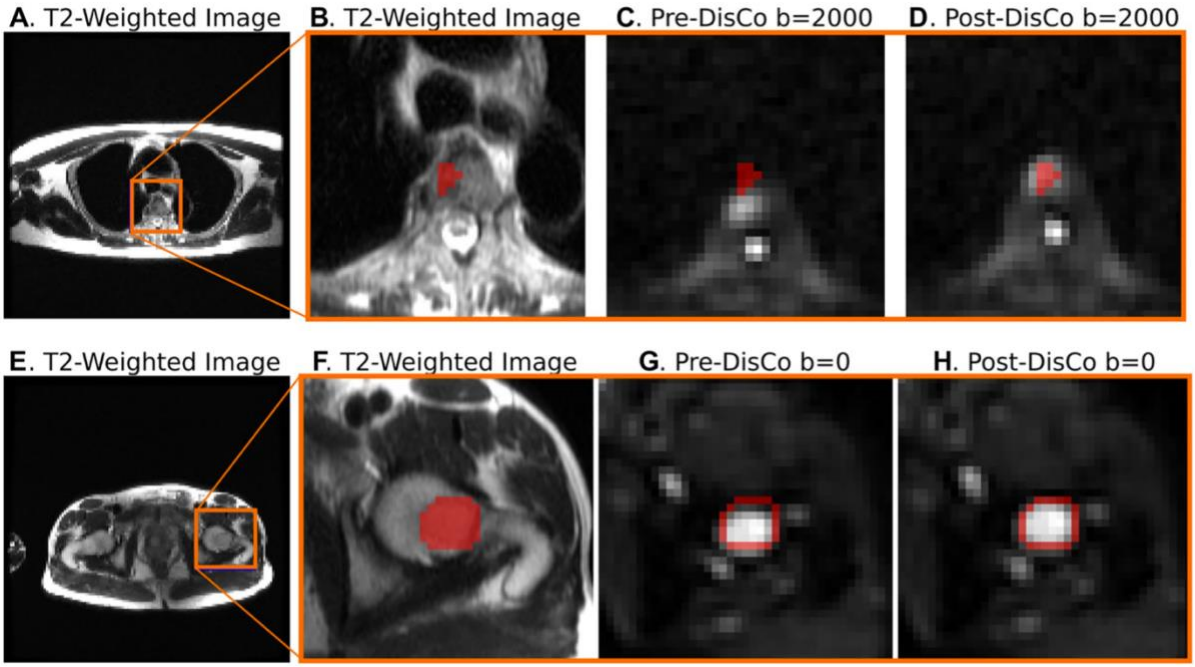

Fig. 13. Assessment of bone metastasis displacement. (A, B, C, D) T2 weighted images. (C, G) Non-distortion corrected images. (D, H) Distortion corrected images [27, p. 5]

The ADC map is also affected by geometric distortions, thus the ADC map from uncorrected diffusion images can be compared with distortion corrected ADC maps as an additional quantitative evaluation method.

Qualitative methods involve subjective visual evaluation of spine misalignment and overall image quality by experienced radiologists [17]. Some examples include: notable image distortion, lesion conspicuity, contrast difference between lesions and adjacent healthy tissue, spatial alignment between imaging stations, and general amount of imaging artifacts. The 5-point Likert scale is a grading tool which can be used to score the different qualitative evaluation criteria.

2.4 Conclusion

WBDWI is performed by the application of linear gradient pulses, which leave the phase of the nuclei altered if they are diffusing freely. When diffusion is restricted, the phase remains unchanged, which results in a different contrast on the MR image [1], [4]. The contrast of tissue on the diffusion image allows a differentiation to be made between diseases.

WBDWI is accompanied with several difficulties, main magnetic field inhomogeneities occur as soon as an object enters the magnetic field due to the magnetic properties of the object. The magnetic properties of air differ greatly when compared to tissue, for this reason, magnetic field inhomogeneities are more prominent near tissue/air borders [1]. Main magnetic field inhomogeneities result in a voxel position shift. The position shift can be resolved by constructing a displacement map from an obtained inhomogeneity field, a technique called “field mapping” [18]. Whole-body diffusion scans are typically performed using EPI sequences which are very susceptible to magnetic field inhomogeneities because of the long readout length and single excitation pulse application. The gradient pulses show non-linear behavior resulting in a magnetic field inhomogeneity, exactly the phenomenon EPI sequences are very

sensitive to. Gradient-induced magnetic field inhomogeneities also cause geometric distortion artifacts which can be resolved by the RPG method [19]. Both the field mapping and RPG methods are combined in a single inline tool called “EPIC”, made by Phillips. The performance of EPIC is well-known in brain examinations but remains unexplored for whole-body applications.

Whole-body scans also show other additional difficulties, such as inter-station intensity variations and inter-station misalignment [26]. Various methods have been developed and tested to correct for these additional difficulties [26], [27], [28]. After correcting distortions and other artifacts, image quality assessment is performed. There are many performance assessment methods available, both quantitative and qualitative [17], [29]. The choice depends on the goal of the study, a combination of methods or altered methods can be used if preferred.

3 Practical study

The importance of distortion correction in WBDWI has been highlighted in the previous chapter. This chapter explains how distortion correction will be implemented and evaluated in practice for this study. Furthermore, the different objectives and steps to complete these goals will be discussed. The design of this study is prospective cross-sectional observational. This practical study is performed at the University hospital of Leuven, "UZ Leuven". An application for the ethics committee was submitted by UZ Leuven using a dedicated protocol [30]. The study is funded by the UZ Leuven department of Radiology which will cover volunteer fees, data storage, transfer, analysis, and publication.

3.1 Objectives

The primary objective of this project is to underscore the significance of echo-planar imaging (EPI) distortion correction (DC) in whole-body diffusion weighted imaging (WBDWI) scans. The outcomes will be instrumental in refining the precision, reliability, and clinical relevance of DWI, ultimately benefiting the management of all patients in need of a WBDWI scan. To complete the primary objective, the following secondary objectives are set:

a. **embedding an adjusted WBDWI sequence into a whole-body protocol,**

b. **perform pilot scans on healthy volunteers to test and optimize the implementation of EPIC,**

c. **quantitative evaluation and comparison of EPIC and non-EPIC in healthy volunteer data:**

    i. **apparent diffusion coefficient values of tissues in each station,**

    ii. **signal-to-noise ratio of corrected and uncorrected images in each station,**

    iii. **distortion of the spinal cord with respect to undistorted T2-weighted images,**

    iv. **inter-station alignment of corrected and uncorrected images,**

    v. **mutual information of segmented structures with respect to T2-weighted images.**

3.2 Materials and methods

One research MRI scanner is used, the scanner is a 3 T MRI machine (Achieva dStream, Philips Medical Systems, Best, The Netherlands) located at the UZ Leuven, campus Gasthuisberg, Leuven, Belgium. This machine will be used to scan healthy volunteers for scan protocol optimization purposes and quantitative image quality assessment.

3.2.1 Scan protocol

The standard scan protocol for this study is shown in table 1, where the diffusion sequence will be modified to support EPIC. In this way, the adjusted DWI sequence is implemented in an existing whole-body protocol. Briefly, the following sequences will be included: axial free-breathing DWI in four imaging stations (head/neck, thorax, abdomen and pelvis) at $b = 0$ and $b = 1000$ s/mm^2 with antero-posterior PE direction. Coronal free-breathing single shot fast spin echo (TSE) T2-weighted images and breath-hold 3D T1-weighted spoiled gradient-echo sequences for thorax, abdomen and pelvis. EPIC will be applied on-scanner and raw data saved for delayed reconstruction to acquire the uncorrected (non-EPIC) diffusion data. Image acquisition acceleration methods such as Compressed-SENSE (CS) and/or multi-band SENSE (MB) will be utilized where feasible.

Table 1: Scan protocol sequences and parameters

	DWI	**T2 SSTSE**	**3D T1 gradient-echo**		
	Axial	Coronal	Axial	Coronal	Axial
Image stations head to mid-thigh	4	3	Abdomen and pelvis (2)	Abdomen and pelvis (2)	Chest (1)
Respiration	Free breathing	respiratory	15 s breath-hold	15 s breath-hold	15 s breath-hold
Fat suppression	STIR (TI = 250 ms)	None	SPAIR	SPAIR	SPAIR
b-values (s/mm2)	0–1000	None	None	None	None
Parallel imaging factor	2.5	4	2	2	2
Repetition time (TR) (ms)	8454	3000	3.6	3.6	3.2
Echo time (TE) (ms)	67	87	1.25–2.20	1.25–2.20	1.5
Slice thickness (mm)	5	6	2.5	2.5	2.5
Slice number	50/station	35/station	90	133	148
Intersection gap (mm)	0.1	0.6	0	0	0
Field of view (FOV) (mm)	420 × 329	375 × 447	375 × 304	400 × 352	375 × 304
Acquired voxel size (mm)	4.57 × 4.71	1 × 1	1.49 × 1.5	1.49 × 1.5	1.49 × 1.5
Reconstructed voxel size (mm)	2.19 × 2.16	0.93 × 0.93	0.71 × 0.71	0.71 × 0.71	0.98 × 0.97

3.2.2 Scan population

This study is conducted on three healthy volunteers, post which the data will be analyzed to compare the results from EPIC to non-EPIC images, and to optimize the scan protocol. Healthy volunteers must have no history of absolute contraindications to MRI or presence of metallic implants that could interfere with the magnetic field or affect image quality. The modification to acquisition parameters required for this study are expected to add about 60 seconds for EPIC per station. For a total of four scan stations, about 4 - 6 mins of additional scan time might be required per participant. All participants must sign an informed consent before commencing the study.

3.2.3 Quantitative image analysis of EPIC compared to non-EPIC

Comparison of EPIC to non-EPIC sequences: both the EPIC and standard sequences will undergo quantitative evaluations to determine their efficacy. All quantitative evaluations are performed using MATLAB® (version R2022b). The diffusion scans are acquired in four separate stations, from station 1 to 4 respectively: pelvis, abdomen, thorax, and head/neck. These names will be used to refer to the station of interest from hereon.

3.2.4 Evaluation of the apparent diffusion coefficient map

Quantitative evaluation of the impact of EPI distortion correction was performed using MATLAB® (version: R2022b). For each volunteer, ADC maps were automatically calculated on the scanner (in-line) for EPIC and non-EPIC diffusion images. Whole-body scans involve four imaging stations, in each station three consecutive slices of the scan volume are selected, where freehand regions of interest are drawn to select a tissue/organ and to retrieve its mean ADC value. Ranging from station one to four, Fig. 14 shows the selected tissues: (a) gluteal muscle, (b) lumbar spinal canal, (c) paraspinal muscle, (d) cervical spinal canal.

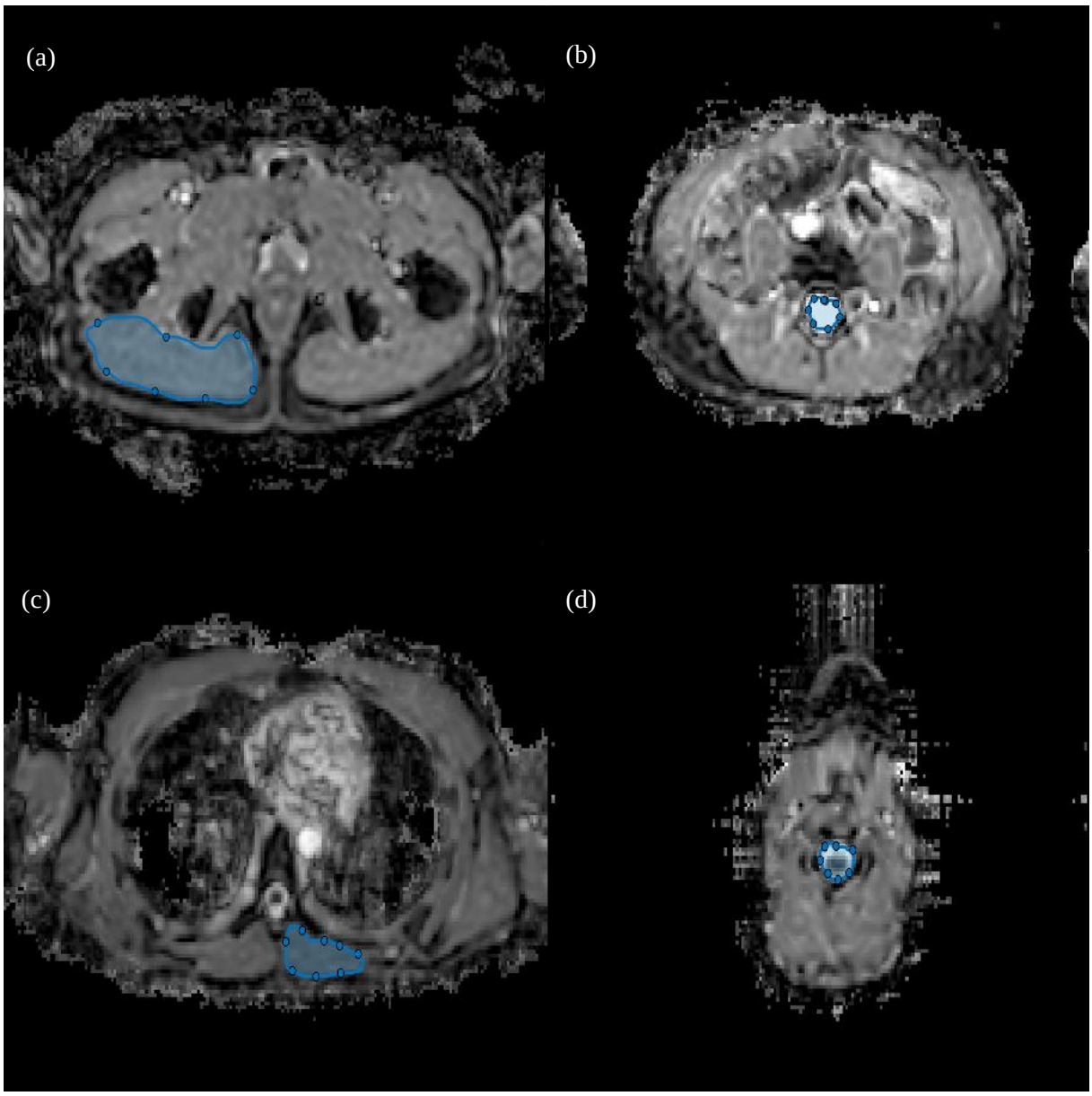

Fig. 14. ROI placement for ADC measurements. Non-EPIC ADC images show (a) gluteal muscle, (b) lumbar spinal canal, (c) spinal muscle, and (d) cervical spinal canal

3.2.5 Impact of EPIC on signal-to-noise ratio

In a similar way to the quantitative approach used to evaluate the effect on ADC values, signal-to-noise ratio is calculated based on the standard deviation of the background and mean signal in tissue. Three consecutive axial slices are used in healthy tissues in each station. In the first station, the prostate is selected as a tissue of interest. In the second, third, and fourth station the freehand ROI is placed on the spinal canal. In the uncorrected image, a circular ROI is used to calculate standard deviation (noise) and the freehand ROI for the mean signal in tissue. The EPIC method uses a threshold which eliminates background noise, to calculate to SNR for EPIC images, the measured noise of the uncorrected image is used. Fig. 15 shows the procedure of SNR calculation of the prostate using MATLAB® (version: R2022b).

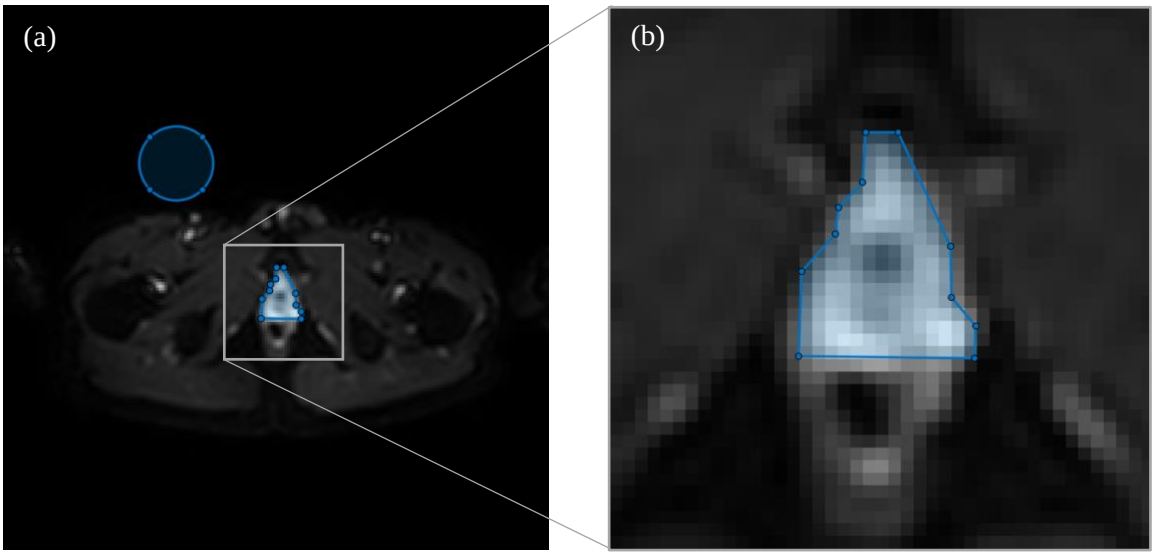

Fig. 15. SNR calculation procedure for the prostate in MATLAB. (a) Circular ROI for noise calculation on the uncorrected image. (b) Polyline ROI for mean signal calculation

3.2.6 Position of the thoracic spinal cord

The thoracic spinal cord is selected as an anatomical landmark for distortion correction evaluation because of its conspicuity on both T2 and b0 diffusion images. Fig. 16 shows the middle slice of a sagittal T2 (a), uncorrected b0 diffusion (b) and corrected b0 diffusion (c) image. A polyline tracing the evaluated section is marked on both images. For the uncorrected and corrected images, 30 consecutive axial slices are evaluated in terms of Euclidian distance using the pdist2() tool from MATLAB®. The absolute value of the distances is used as a means to describe the positional difference.

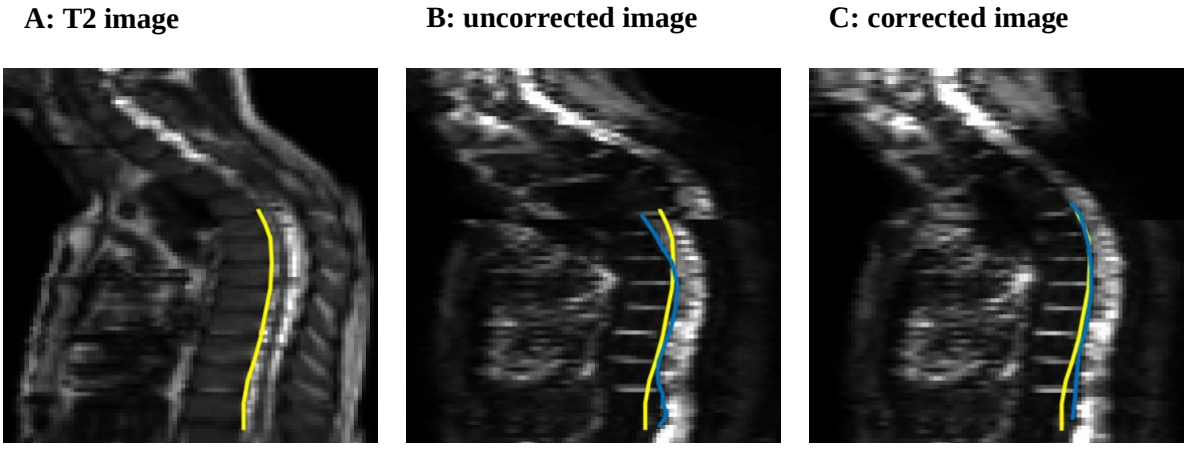

Fig. 16. Sagittal slice of the thoracic station. Section marked for the evaluation of positional difference between T2 (A), uncorrected diffusion (B) and corrected diffusion (C) images. Yellow line is a section of the delineation of the anterior spinal cord on the T2 image, blue lines trace the same structure on the diffusion images

3.2.7 Impact of EPIC on inter-station alignment

The inter-station alignment is evaluated for both corrected and uncorrected images by calculating the absolute distance (antero-posterior direction) between a red point marking the anterior spinal cord on one axial slice, and a blue point marked on the next axial slice. This is done for six consecutive slices. Fig. 17 shows the principle for both corrected and uncorrected b0 and b1000 images, the example shows an uncorrected image.

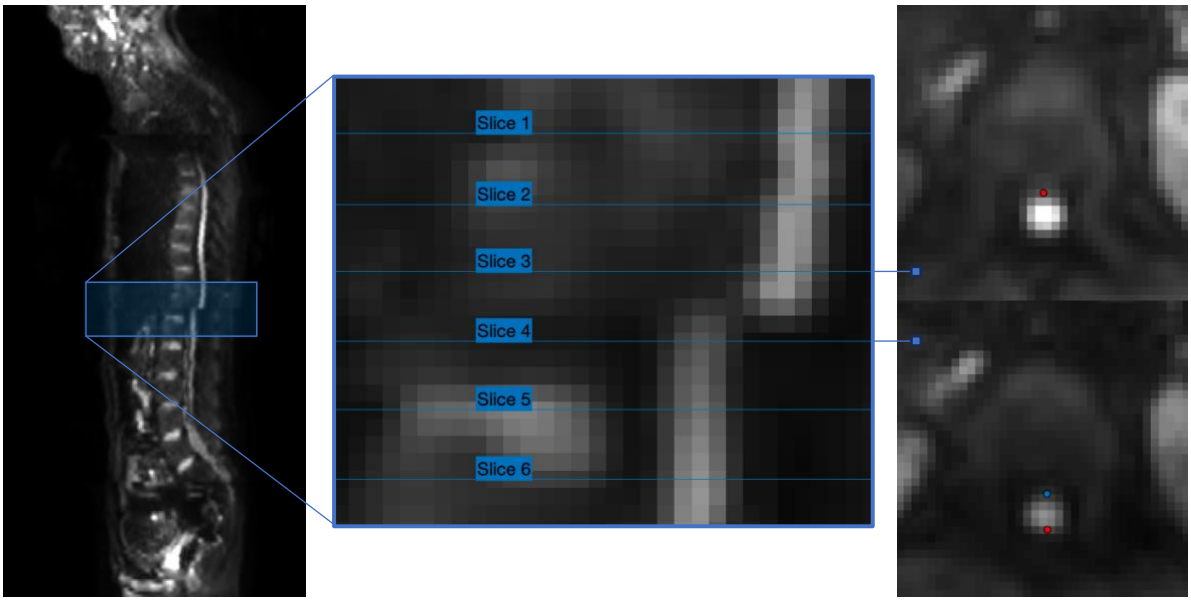

Fig. 17. Inter-station alignment evaluation for uncorrected and corrected diffusion images. For a total of six slices, on each slice a red marker is placed marking the anterior portion of the spinal cord, the red marker is then copied to a consecutive slice on which a blue marker is used to mark the same anatomic landmark. After marking two consecutive slices, the absolute value between the distances of the markers is calculated

3.2.8 Similarity of segmented structures

The effect of distortion correction on the position of structures is evaluated by calculating the mutual information between corrected, uncorrected, and structural T2 images in MATLAB®. To be able to compare T2 and diffusion data, images were registered using an affine transformation. Mutual information between the segmented structures is then calculated by using the mi() function created by [31], based on the theory explained in [32]. In each station, several structures are selected to segment, through three consecutive slices. In station 1 to 4 respectively, the following structures are segmented: gluteal muscle, left kidney, paraspinal muscle, and spinal canal. As an example, the left kidney is selected in five consecutive axial slices for T2, b0 and b1000 diffusion images. Fig. 18 shows the principle, were (a) is the T2, (b) the corrected and (c) the uncorrected image.

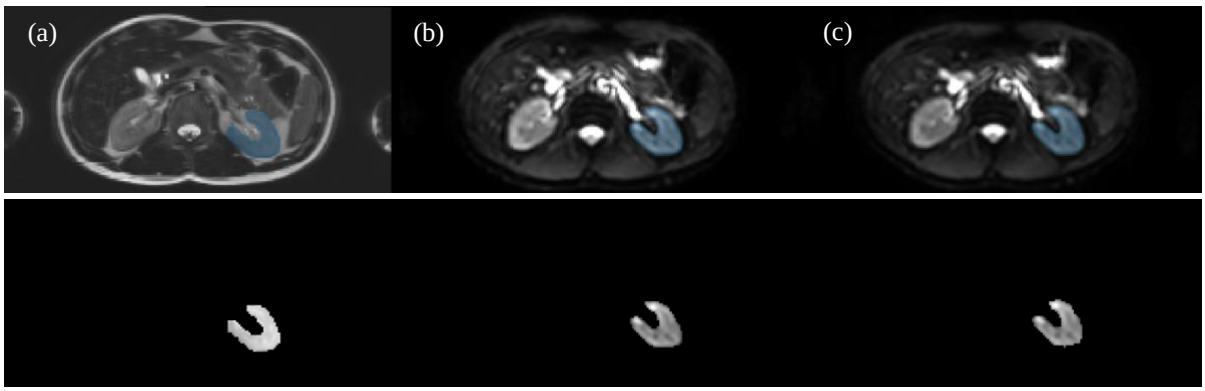

Fig. 18. Procedure to calculate mutual information for station 2. Top row: (a) T2 structural image, (b) EPIC b0 diffusion image, (c) non-EPIC b0 diffusion image. Bottom row: segmented left kidney for (a), (b), and (c) respectively

3.3 Results

3.3.1 Implementation of EPIC and study population

EPIC is successfully implemented into the diffusion sequence of the whole-body protocol. To be able to implement EPIC into the diffusion sequence of the whole-body protocol, only a few changes have to be accepted regarding the diffusion sequence. A b0 field map and a blip-up blip-down EPI pair have to be collected. A research patch allowed EPIC to be activated for whole-body purposes. Three healthy volunteers participated in this study and no incidental findings were found during the scan sessions, all scans are fully completed.

3.3.2 Comparison of the ADC map

Results of ADC measurements from the first, second, and third dataset are summarized and shown in table 2. The percent difference is calculated using equation 7:

$$Percent\ difference = \frac{|a-b|}{(a+b)/2} * 100 \tag{7}$$

In equation 7, a and b are the EPIC and non-EPIC value, respectively. The standard deviation (σ) of the mean value, as well as the mean standard deviation inside the ROIs (σ_{ROI}) is reported in the table.

Table 2: Mean of ADC measurement results

Station	Non-EPIC ADC value ± σ [$\times 10^{-6}$ mm^2/s]	Non-EPIC σ_{ROI} [$\times 10^{-6}$ mm^2/s]	EPIC ADC value ± σ [$\times 10^{-6}$ mm^2/s]	EPIC σ_{ROI} [$\times 10^{-6}$ mm^2/s]	Percent difference ± σ [%]
Pelvis	162 ± 6.03	10.9	162 ± 6.51	12.8	0.300 ± 0.175
Abdomen	329 ± 31.5	38.0	330 ± 32.9	41.6	0.737 ± 0.657
Thorax	166 ± 3.61	11.5	165 ± 3.51	14.4	0.831 ± 0.451
Head/neck	253 ± 20.1	77.1	245 ± 18.0	76.8	3.42 ± 1.15

A maximum mean percent difference (± σ) of 3.42% (± 1.15%) is measured in the fourth station, with the greatest value originating from the third dataset (4.48%). The largest standard deviation inside the ROIs is found in the fourth station, with the values of non-EPIC and EPIC being nearly equal: 77.1×10^{-6} mm^2/s and 76.8×10^{-6} mm^2/s, respectively. The greatest standard deviation of the values is found in the abdominal station, with values of non-EPIC and EPIC being nearly equal: 31.5×10^{-6} mm^2/s and 32.9×10^{-6} mm^2/s, respectively.

3.3.3 SNR measurements

The measured SNR of b0 diffusion scans in EPIC and non-EPIC image series is shown in table 3, 4, and 5, for dataset 1, 2, and 3 respectively. Table 6, 7, and 8 show the SNR data for b1000 diffusion scans in dataset 1, 2, and 3 respectively.

Table 3: Result of b0 SNR measurements in dataset 1

Station	Non-EPIC SNR	EPIC SNR	Standard deviation	Percent difference [%]
Pelvis	2.25×10^3	2.23×10^3	7.42	1.16 (-)
Abdomen	3.93×10^3	3.94×10^3	9.04	0.178
Thorax	2.18×10^3	2.05×10^3	5.18	6.37 (-)
Head/neck	2.85×10^3	3.01×10^3	1.71	5.33

Table 4: Result of b0 SNR measurements in dataset 2

Station	Non-EPIC SNR	EPIC SNR	Standard deviation	Percent difference [%]
Pelvis	1.45×10^3	1.42×10^3	12.7	2.32 (-)
Abdomen	2.20×10^3	2.13×10^3	23.9	3.27 (-)
Thorax	797	1.16×10^3	4.26	36.9
Head/neck	320	294	1.16	8.61 (-)

Table 5: Result of b0 SNR measurements in dataset 3

Station	Non-EPIC SNR	EPIC SNR	Standard deviation	Percent difference [%]
Pelvis	2.08×10^3	2.42×10^3	2.79	14.9
Abdomen	4.47×10^3	5.56×10^3	7.02	21.7
Thorax	1.92×10^3	1.68×10^3	3.76	13.2 (-)
Head/neck	4.41×10^3	4.97×10^3	1.10	11.9

In 50% of all cases for b0 imaging data, the SNR is increased by applying EPIC. The negative SNR change in b0 corrected images due to EPIC can be low (< 6.37%), but negative changes of up to 13.2% have also been measured. Positive SNR changes of up to 36.9% have been measured for the thoracic station, while maximum positive changes of 14.9%, 21.7%, and 11.9% were found for stations 1, 2, and 4, respectively. The greatest mean percent difference ($\pm \sigma$) is found in the thoracic station, i.e. 18.8% ($\pm$ 16.0%). In other stations, the mean percent difference is less than 8.62%.

Table 6: Result of b1000 SNR measurements in dataset 1

Station	Non-EPIC SNR	EPIC SNR	Standard deviation	Percent difference [%]
Pelvis	577	568	4.12	1.65 (-)
Abdomen	163	161	1.88	1.49 (-)
Thorax	287	290	1.88	1.05
Head/neck	774	819	0.660	5.61

Table 7: Result of b1000 SNR measurements in dataset 2

Station	Non-EPIC SNR	EPIC SNR	Standard deviation	Percent difference [%]
Pelvis	307	295	0.746	3.76 (-)
Abdomen	153	151	3.73	1.85 (-)
Thorax	86.4	157	0.305	57.8
Head/neck	58.9	57.0	0.224	3.35 (-)

Table 8: Result of b1000 SNR measurements in dataset 3

Station	Non-EPIC SNR	EPIC SNR	Standard deviation	Percent difference [%]
Pelvis	531	615	1.61	14.5
Abdomen	143	173	1.11	19.5
Thorax	290	331	3.35	13.1
Head/neck	894	1.08×10^3	2.33	19.3

Regarding b1000 diffusion images, in 41.7% of all cases the SNR is decreased. The largest negative SNR change for b1000 imaging data is 3.76%, which would generally not be noticed without quantitative measurement. The largest positive change (57.8%) has again been recorded in the thoracic station. Positive SNR changes of up to 14.5%, 19.5%, and 19.3% have been measured in stations 1, 2, and 4, respectively. The greatest mean percent difference ($\pm \sigma$) of all datasets is found in the thoracic station, i.e. 24.0% ($\pm$ 29.9%). In other stations, the mean percent difference is less than 9.42%.

3.3.4 Positional difference of the thoracic spinal cord

Regarding the difference between the position of the anterior part of the spinal cord, the mean of the absolute distance between T2 markers and diffusion image markers was calculated, table 9 shows the results.

Table 9: Results for positional difference measurements

	Mean distance [pixels] (EPIC)	Mean distance [pixels] (Non-EPIC)
Dataset 1	0.5695	1.7159
Dataset 2	1.3959	1.6061
Dataset 3	1.0547	1.7108
Total mean	1.0067	1.6776

The mean difference between EPIC distances and non-EPIC distances is 0.6709 pixels (1.47 mm), which corresponds to an improvement of 60%.

3.3.5 Inter-station alignment

Results of the inter-station alignment measurements for volunteer 1 are given in table 10, for b0 and b1000 EPIC and non-EPIC data. Table 11 and 12 show the results for the second and third volunteer respectively. Section 3 represents the traversing of stations, as explained in the methods section. Distances in pixels can be multiplied by 2.1875 mm per pixel to convert to mm.

Table 10: Results of inter-station alignment measurements for dataset 1

Dataset 1 b0						
Section	**1**	**2**	**3**	**4**	**5**	**6**
Mean of absolute distances (non-EPIC; EPIC) [pixels]	1.024; 0.007491	0.01874; 0.01940	5.962; 4.054	0.02115; 0.02320	0.02835; 0.2540	2.0375; 1.983
Dataset 1 b1000						
Mean of absolute distances (non-EPIC; EPIC) [pixels]	0.009074; 0.02205	0.015156; 0.01878	4.981; 2.984	0.9654; 0.9893	0.008936; 0.01698	0.9400; 0.5079

Table 11: Results of inter-station alignment measurements for dataset 2

Dataset 2 b0						
Section	**1**	**2**	**3**	**4**	**5**	**6**
Mean of absolute distances (non-EPIC; EPIC) [pixels]	0.03387; 0.03777	0.01296; 0.09795	4.931; 0.042520	0.9776; 0.9836	0; 0.05169	0.7183; 0.02614
Dataset 2 b1000						
Mean of absolute distances (non-EPIC; EPIC) [pixels]	0.008892; 0.01437	0.04333; 0.03460	2.984; 0.01984	0.0477; 0.03285	0.02853; 0.01366	0.0110; 0.02700

Table 12: Results of inter-station alignment measurements for dataset 3

Dataset 3 b0						
Section	**1**	**2**	**3**	**4**	**5**	**6**
Mean of absolute distances (non-EPIC; EPIC) [pixels]	1.0079; 0.9070	0.9507; 0.9540	2.9604; 2.0118	0.0328; 1.0532	0.0331; 0.0336	0.0465; 0.0342
Dataset 3 b1000						
Mean of absolute distances (non-EPIC; EPIC) [pixels]	0.0101; 0.0328	0.0197; 0.0461	0.9438; 0.9082	0.0073; 0.0189	1.0186; 0.0043	0.0153; 0.0423

These results show a larger absolute distance at section 3, where stations are stitched together. The mean inter-station misalignment reduction of b0 and b1000 data is 54.4% and 47.7%, respectively. The maximum reduction is 99.1% and 99.3% for b0 and b1000 data respectively. The average reduction of misalignment for all b-values is 51.1%.

3.3.6 Similarity of segmented structures

Concerning the similarity between the position of structures, results of mutual information (MI) measurements between segmented T2, uncorrected, and corrected structures is shown in table 13 and 14

for b0 and b1000 data respectively. Values represent the mean MI of measurements on three consecutive slices.

Table 13: Results of MI measurements for b0 diffusion images

b = 0	**Dataset 1**		**Dataset 2**		**Dataset 3**	
Station	**EPIC**	**Non-EPIC**	**EPIC**	**Non-EPIC**	**EPIC**	**Non-EPIC**
1	0.165	0.167	0.200	0.194	0.172	0.163
2	0.0390	0.0455	0.0918	0.0887	0.0918	0.0882
3	0.0526	0.0428	0.0263	0.0254	0.0975	0.0915
4	0.0782	0.0780	0.0097	0.0055	0.0129	0.00830
Mean difference (EPIC – Non-EPIC)	0.000375		0.00355		0.0058	

The mean of all stations show higher values for EPIC images, for all datasets. The total mean difference of MI for all stations and all b0 datasets is 0.00324.

Table 14: Results of MI measurements for b1000 diffusion images

b = 1000	**Dataset 1**		**Dataset 2**		**Dataset 3**	
Station	**EPIC**	**Non-EPIC**	**EPIC**	**Non-EPIC**	**EPIC**	**Non-EPIC**
1	0.134	0.131	0.158	0.153	0.0551	0.0322
2	0.0308	0.0305	0.0860	0.0785	0.0669	0.0545
3	0.0487	0.0412	0.0289	0.0239	0.0392	0.0355
4	0.00749	0.00845	0.00344	0.00152	0.00258	0.000904
Mean difference (EPIC – Non-EPIC)	0.00246		0.198		0.0102	

The mean of all stations show higher values for EPIC images, for all datasets. The total mean difference of MI for all station and all b1000 datasets is 0.0703. The total mean difference for all b-values and all datasets is 0.037.

3.3.7 Scan protocol optimization

After quantitative image analysis of two datasets, the scan protocol was updated. The new protocol is shown in table 15, with parameter changes marked in bold. Imaging data from the second volunteer showed black bands in certain regions. This was assumed to be due to an error regarding the resolution of the b0 prescan, which ultimately affects the SNR and is relevant for the noise cut-off feature of EPIC. To resolve this issue, the b0 prescan resolution is first changed from 3x3x3 to 4x4x4 to increase SNR. Because the resolution of the b0 prescan is changed, the prescan could only work if the slice thickness of the diffusion sequences were changed from 5 mm to 4 mm. Changing the slice thickness without altering the number of slices acquired would have changed the total scan volume, to compensate for this effect, the total number of acquired slices was changed from 50 to 62. Another change was made to the slice encoding (SE) direction of the T2 sequence. For the third dataset, the slice encoding direction was changed to axial to simplify image registration techniques. Quantitative evaluation of the third dataset is performed identical to the evaluation of the first two datasets, as the main objective is to compare

EPIC to non-EPIC, and structural images. There was no presence of black bands in the images of the dataset scanned with the updated protocol.

Table 15: Updated scan protocol, changes marked in bold and italic

	DWI	**T2 SSTSE**	**3D T1 gradient-echo**		
	Axial	***Axial (was coronal)***	Axial	Coronal	Axial
Image stations head to mid-thigh	4	3	Abdomen and pelvis (2)	Abdomen and pelvis (2)	Chest (1)
Respiration	Free breathing	respiratory	15 s breath-hold	15 s breath-hold	15 s breath-hold
Fat suppression	STIR (TI = 250 ms)	None	SPAIR	SPAIR	SPAIR
b-values (s/mm2)	0–1000	None	None	None	None
Parallel imaging factor	2.5	4	2	2	2
Repetition time (TR) (ms)	8454	3000	3.6	3.6	3.2
Echo time (TE) (ms)	67	87	1.25–2.20	1.25–2.20	1.5
Slice thickness (mm)	**4 (was 5)**	6	2.5	2.5	2.5
Slice number	**62/station (was 50/station)**	35/station	90	133	148
Intersection gap (mm)	0.1	0.6	0	0	0
Field of view (FOV) (mm)	420 × 329	375 × 447	375 × 304	400 × 352	375 × 304
Acquired voxel size (mm)	4.57 × 4.71	1 × 1	1.49 × 1.5	1.49 × 1.5	1.49 × 1.5
Reconstructed voxel size (mm)	2.19 × 2.16	0.93 × 0.93	0.71 × 0.71	0.71 × 0.71	0.98 × 0.97

3.4 Discussion

3.4.1 Limitations

Due to time considerations and delay concerning the ethics committee approval, the size of the volunteer group is small (N = 3), which is a limitation of this study. The recruited volunteers were scanned under a general informed consent. Although the study size is limited, the diffusion sequences in the whole-body protocol acquire b0 and b1000 weighted images, which increases the available data for image quality assessment. Because a b0 and b1000 gradient strength is used, ADC maps were also calculated which allowed for additional quantitative comparisons to be made between EPIC and non-EPIC images. The whole-body diffusion sequence is acquired in four sections, which allows an additional comparison to be made between the stations. Three volunteers have been recruited, which is the predetermined size for scan protocol optimization purposes and first image quality assessment.

3.4.2 Implementation of EPIC

EPIC was successfully implemented in this thesis by introducing a research patch and accepting a b0 field map and BUBD EPI pair acquisition. No scan conflicts were found and no other parameters had to be adjusted. EPIC for whole-body purposes requires no post-processing and is therefore a very easy to apply distortion correction method, which requires no knowledge of the technique itself. In non-research oriented centers, the operator will typically have no knowledge of post-processing techniques, which were necessary before EPIC was introduced and tested for whole-body scans. The results of this thesis demonstrate the effectiveness and benefits of EPIC as an inline tool for applying distortion correction in whole-body scans. Furthermore, this thesis has investigated EPIC using a Philips scanner, but the concept can also be applied to other vendors in the same way.

3.4.3 Quantitative evaluation

ADC-comparison. The largest mean percent difference of ADC values ($\pm \sigma$) is measured in the fourth station, being equal to 3.42% ($\pm$ 1.15%). The greatest individual percent difference of a dataset is 4.48%, also in the fourth station. The standard deviation inside the ROIs of the fourth station is also the greatest, which means a large difference in ADC values in the ROIs is present. This can be explained by the fact that the nerves of the cervical spinal canal are partially included in the ROI, as seen on Fig. 16d. Avoiding the nerves in this case is difficult and depends on multiple factors, such as the curvature of the participant, size of the cervical anatomy, and slice thickness. A smaller ROI measuring ADC of the nerves or cerebrospinal fluid only could possibly be used to avoid this, but this was not tested. The fourth station corresponds to the head/neck area which is known to be an area prone to patient induced artifacts such as motion artifacts from swallowing. If more geometric distortion is present in the head neck area, a larger correction from EPIC will be applied to the images, leading to a greater difference between EPIC and non-EPIC ADC images. It would be assumed that EPIC does not correct for patient induced movement but these results indicate that a greater correction is applied in areas prone to patient induced movement. A dedicated head/neck distortion correction study [21] found a non-significant difference of 1% in ADC values. A Wilcoxon signed ranked test ($p = 0.05$) is performed on this data using the

MATLAB® function signrank(), resulting in p-values higher than 0.25 for all stations. The p-value may be the result of the small study size, but different independent studies [17], [21] with larger groups also found the difference to be insignificant. Thus, the ADC difference between EPIC and non-EPIC images is not significant. To summarize, the difference in ADC values between corrected and uncorrected images is small (< 4.5%) and not significant ($p \geq 0.25$), which was also demonstrated by the results of [17] and [21].

SNR values. Results show that the greatest difference occurs in the thoracic station, for b0 data the mean percent difference ($\pm \sigma$) is 18.8% ($\pm$ 16.0%) and for b1000 data 24% ($\pm$ 29.9%). The larger difference in b1000 data could be due to the use of a stronger gradient, which increases the distortion of the resulting image. In other stations, the mean percent difference is less than 8.62% and 9.42% for b0 and b1000 data respectively. The b0 data shows that in 50% of all cases for b0 imaging data, the SNR is decreased with negative changes of up to 13.2%, which may affect image quality. Notable positive SNR changes of up to 36.9% have been measured for the thoracic station. Regarding b1000 diffusion images, in the majority of cases (58.3%) the SNR is increased. The largest negative SNR change for b1000 imaging data (3.76%) would generally not be noticed without quantitative measurement. The largest positive change (57.8%) has again been recorded in the thoracic station. Positive SNR changes of up to 14.5%, 19.5%, and 19.3% have been measured in station 1, 2, and 4, respectively. The thoracic station is very susceptible to patient induced motion artifacts, which can be caused by coughing for example. Off-resonance fields are known to influence the SNR by inducing a signal loss. If the resonant frequencies of voxels inside a ROI have a large standard deviation, the dephasing (T2*) effect will be greater and in this way induce a signal loss on the resulting image [33]. It could be assumed that the distortion correction does not correct for this signal loss because the signal loss is already present before correction and cannot be prevented. The faster dephasing will have already taken place, the only way mean signal could be increased due to correction is the mapping of non-zero intensity voxels inside the distorted area, replacing zero intensity voxels and in this way increase the mean signal. Off-resonance voxels originating from tissue/air boundaries could be mapped into tissue, for example a zero intensity value voxel (air) mapped into a non-zero tissue such as muscle will reduce the mean signal of that tissue. The SNR of images is not the most important factor when the decision is made to apply distortion correction, the most important aspect would be the geometric distortion. There are limited resources in the literature regarding the effect on SNR of EPI distortion correction. Generally, b1000 data indicates a large positive SNR change of up to 57.8%, or a small negative SNR change ($\leq$ 3.76%) is possible, with a general positive change being noticed in 58.3% of all cases. Therefore, if the SNR of b1000 data is an important criteria, the decision must be made to use EPIC as the possible benefits greatly outweigh the risks. Summarizing the b0 data, positive SNR changes of up to 36.9% have been measured, but negative changes of up to 13.2% are also possible, with an equal chance of a general positive or negative change being present. For b0 data the benefits are also greater than the risks, but a possible negative change of 13.2% in SNR must be kept in mind. Because it is not possible to activate EPIC for b1000 and not for b0 images, the general conclusion is that the possible benefits of applying EPIC outweigh the risks, therefore recommending the use of EPIC in terms of SNR.

Positional difference of the thoracic spinal cord. The mean distance between markers on diffusion images and T2 weighted images is reduced by 60% (0.6709 pixels), which proves the efficacy of EPIC. The pixel width and height of all axial diffusion images is 2.1875 mm/pixel. A mean distance of 0.6709 pixels corresponds to 1.47 mm. Depending on the specific indication of the examination, a change of 1.47 mm could be significant. The results of [29] show a larger error reduction (11.8 mm), but in that study a portion of the cervical spine was also traced, which is not the case in this study. Tracing through

stations from the bottom of the thoracic station to the mid head/neck station would indeed yield much larger error reductions which can already be seen from Fig. 18, where the specific method for this study is explained. The future goal is to test and evaluate the protocol on a clinical population with known breast cancer/multiple myeloma. Breast cancer is known to be able to cause distant metastases in 20 – 30% of early-stage patients [34], with the majority (≥ 65%) of metastases occurring in bone [35]. Knowing this, small geometric error reductions can be of great importance in locating distant metastases. Based on these results, it is clear that the application of EPIC improves positional correlation with respect to undistorted T2 images.

Inter-station alignment. The EPIC-corrected images have better inter-station alignment, with a large difference between corrected and uncorrected images in dataset 2 for b0 and b1000 data. The largest corrections were applied in dataset 2, where misalignments are reduced by 99.1% and 99.3% for b0 and b1000 data respectively. In dataset 2, the applied correction practically eliminates the inter-station misalignment, making them completely aligned as in undistorted images. The average misalignment reduction for all b-values is 51.1%, which corresponds to a distance of 4.65 mm. Following the same reasoning as in the previous subsection about the positional difference of the thoracic spinal cord, this could be of great importance in locating distant bone metastases in tissue. The effect is even more pronounced at the intersection of the thoracic and head/neck station as seen in Fig. 18. If a bone metastasis would be located at this interface, partially in the thoracic station and partially in the head/neck station, the metastasis would be greatly deformed and displaced when no distortion correction is applied. This demonstrates the usefulness of EPIC in correcting inter-station misalignment for whole-body purposes.

Similarity of segmented structures. The mean MI of all stations show higher values for EPIC images, for all datasets. The MI improvement for b1000 imaging data is greater than in b0 data, which is in contrast to the results of [17], where better results were obtained in low b-values (b0 and b50). It is assumed that the effect of distortion correction on MI in [17] is less successful for high b-values due to the stronger gradients and thus larger eddy currents, which were not accounted for in that particular study. These results indicate that EPIC is also successful in correcting greater distortions at higher b-values. To conclude the results of MI measurements, the positions of structures on EPIC images are in better agreement with undistorted T2 images compared to uncorrected diffusion images, for all b-values.

Scan protocol optimization. The protocol is optimized and ready for use on a clinical population, it is tailored for a patient population who are diagnosed with breast cancer/multiple myeloma. The diffusion sequence is of great importance and by using the protocol developed in this thesis, the distortion of the diffusion images is reduced. The protocol also includes a T2 and T1 sequence to enable a differential diagnosis of suspicious tissues or structures.

4 Conclusion

In this work, whole-body echo planar imaging distortion correction is successfully implemented by adapting a diffusion sequence into supporting EPIC, and further optimizing the sequence.

The results show that EPIC does not significantly change the ADC values in tissues, with measured percent differences less than 4.5% between corrected and uncorrected images. Although only small differences were found in ADC values of healthy tissue, the largest difference was found in the head/neck station which is more susceptible to patient motion.

Concerning SNR measurements, the SNR of b1000 images show positive changes of up to 57.8% and maximum negative changes of 3.76%. The probability of a general positive change is 58.3%. For b0 images, positive SNR changes of up to 36.9% have been measured, but negative changes of up to 13.2% are also possible, with an equal probability of a general positive or negative change being present. The general conclusion is that the possible benefits of applying EPIC outweigh the risks, therefore recommending the use of EPIC in terms of SNR.

The application of EPIC improves positional correlation with respect to undistorted T2 images by 60%, measurements of the difference in position between EPIC and non-EPIC images of the thoracic spine show a mean difference of 1.47 mm. Inter-station alignment improved when EPIC is applied, the average improvement for all b-values is 51.1%, which corresponds to a distance of 4.65 mm. Mutual information of b0 and b1000 diffusion images with respect to T2 images is an average of 0.037 greater when EPIC is used.

The results show the benefit of applying EPIC for whole-body purposes. By using the findings from the volunteer scans, the protocol is updated for future use. This dedicated breast cancer/multiple myeloma protocol is ready to be used on a clinical patient population in a future study. This can ultimately improve disease follow up and management of such patients and even allows further adaptation for different clinical indications in the future.

References

[1] P. J. Basser and E. Özarslan, "Introduction to Diffusion," in *Diffusion MRI*, H. Johansen-Berg and T. E.J. Behrens, Eds., Amsterdam, Netherlands: Elsevier, 2014, ch. 1, pp. 3-9.

[2] V. Baliyan, C. J. Das, R. Sharma and A. K. Gupta, "Diffusion weighted imaging: Technique and applications," *World J. Radiol.*, vol. 8, no. 9, pp. 785-798, Sep. 2016, doi: 10.4329/wjr.v8.i9.785.

[3] F. Crop, C. Robert, R. Viard, J. Dumont, M. Kawalko, P. Makala, et al., "Efficiency and Accuracy Evaluation of Multiple Diffusion-Weighted MRI Techniques Across Different Scanners,"*J. Magn. Reson. Imaging.*, vol. 59, no. 1, pp. 311-322, Jun. 2023, doi: 10.1002/jmri.28869.

[4] C. Westbrook and C. Kaut, "Pulse Sequences," in *MRI in Practice*, Hoboken, U.K.: Blackwell Science Ltd, 2000, ch. 5, pp. 104-140.

[5] N. A. Hottat, D. A. Badr, M. B. Ghanem, T. Besse-Hammer, S. M. Lecomte, C. Vansteelandt, et al., "Assessment of whole-body MRI including diffusion-weighted sequences in the initial staging of breast cancer patients at high risk of metastases in comparison with PET-CT: a prospective cohort study," *Eur. Radiol., vol. 34, no. 1, pp. 165-178, Jan.* 2024, doi: 10.1007/s00330-023-10060-0.

[6] C. Messiou, J. Hillengass, S. Delorme, F. E. Lecouvet, L. A. Moulopoulos, D. J. Collins, et al., "Guidelines for Acquisition, Interpretation, and Reporting of Whole-Body MRI in Myeloma: Myeloma Response Assessment and Diagnosis System (MY-RADS)," *Radiology.*, vol. 291, no. 1, pp. 5-13, Apr. 2019, doi: 10.1148/radiol.2019181949.

[7] S. Keaveney, A. Dragan, M. Rata, M. Blackledge, E. Scurr, J. M. Winfield, et al., "Image quality in whole-body MRI using the MY-RADS protocol in a prospective multi-centre multiple myeloma study," Insights Imaging., vol. 14, no. 170, pp. 1-14, Oct. 2023, doi: 10.1186/s13244-023-01498-3.

[8] P. Summers, G. Saia, A. Colombo, P. Pricolo, F. Zugni, S. Alessi, et al., "Whole-body magnetic resonance imaging: technique, guidelines and key applications," *Ecancermedicalscience.*, vol. 15, Jan. 2021, Art. no. 1164, doi: 0.3332/ecancer.2021.1164.

[9] S. Yoshida, T. Takahara, Y. Arita, S. Sakaino, K. Katahira and Y. Fujii, "Whole-body diffusion-weighted magnetic resonance imaging: Diagnosis and follow up of prostate cancer and beyond," *Int. J. Urol.*, vol. 28, no. 5, pp. 502-513, May. 2021, doi: 10.1111/iju.14497.

[10] K. Nakanishi, J. Tanaka, Y. Nakaya, N. Maeda, A. Sakamoto, A. Nakayama, et al., "Whole-body MRI: detecting bone metastases from prostate cancer,"*Jpn. J. Radiol.*, vol. 40, no. 3, pp. 229-244, Oct. 2022, doi: 10.1007/s11604-021-01205-6.

[11] J. Winfield, M. Blackledge, N. Tunariu, D.-M. Koh and C. Messiou, "Whole-body MRI: a practical guide for imaging patients with malignant bone disease," *Clin. Radiol.*, vol. 76, no. 10, pp. 715-727, Oct. 2021, doi: 10.1016/j.crad.2021.04.001.

[12] J. L. Andersson, "Geometric distortions in Diffusion MRI," in *Diffusion MRI*, H. Johansen-Berg and T. E.J. Behrens, Eds., Amsterdam, Netherlands: Elsevier, 2014, ch. 4, pp. 63-85.

[13] J. Pipe, "Pulse Sequences for Diffusion-Weighted MRI," in *Diffusion MRI*, H. Johansen-Berg and T. E.J. Behrens, Eds., Amsterdam, Netherlands: Elsevier, 2014, ch. 2, pp. 11-34.

[14] K. L. Miller, "Diffusion Acquisition: Pushing the Boundaries," in *Diffusion MRI*, H. Johansen-Berg and T. E.J. Behrens, Eds., Amsterdam, Netherlands: Elsevier, 2014, ch. 3, pp. 35-61.

[15] D. Le Bihan, C. Poupon, A. Amadon and F. Lethimonnier, "Artifacts and Pitfalls in Diffusion MRI," *J. Magn. Reson. Imaging.,* vol. 24, no. 3, pp. 478-488, Aug. 2006, doi: 10.1002/jmri.20683.

[16] S. Y. Huang, R. T. Seethamraju, P. Patel, P. F. Hahn, J. E. Kirsch and A. R. Guimaraes, "Body MR Imaging: Artifacts, k-Space, and Solutions," *Radiographics,* vol. 35, no. 5, pp. 1439-1460, Sep-Oct. 2015, doi: 10.1148/rg.2015140289.

[17] T. Sjöholm, J. Kullberg, M. Engström, H. Ahlström and F. Malmberg, "Improved geometric accuracy of whole body diffusion-weighted imaging at 1.5T and 3T using reverse polarity gradients," *Scientific Reports,* vol. 12, 2022, Art. no. 11605, doi: 10.1038/s41598-022-15872-6.

[18] P. Jezzard and R. S. Balaban, "Correction for geometric distortion in echo planar images from B0 field variations," *Magn. Reson. Med.,* vol. 34, no. 1, pp. 65-73, Jul. 1995, doi: 10.1002/mrm.1910340111.

[19] H. Chang and M. J. Fitzpatrick, "A Technique for Accurate Magnetic Resonance Imaging in the Presence of Field Inhomogeneities," *IEEE Trans. Med. Imaging,* vol. 11, no. 3, pp. 319-329, Sep. 1992, doi: 10.1109/42.158935.

[20] B. L. Schmitz, A. J. Aschoff, M. H. Hoffman and G. Grön, "Advantages and Pitfalls in 3T MR Brain Imaging: A Pictorial Review," *Am. J. Neuroradiol.,* vol. 26, no. 9, pp. 2229-2237, Oct. 2005.

[21] R. M. Winter, H. Schmidt, S. Leibfarth, K. Zwirner, S. Welz, N. F. Schwenzer, et al., "Distortion correction of diffusion-weighted magnetic resonance imaging of the head and neck in radiotherapy position," *Acta Oncol.,* vol. 56, no. 11, pp. 1659-1663, Nov. 2017, doi: 10.1080/0284186X.2017.1377347.

[22] G. Nketiah, K. M. Selnæs, E. Sandsmark, J. R. Teruel, B. Krüger-Stokke, H. Bertilsson, et al., "Geometric distortion correction in prostate diffusion-weighted MRI and its effect on quantitative apparent diffusion coefficient analysis," *Magn. Reson. Med.,* vol. 79, no. 5, pp. 2441-2851, May. 2018, doi: 10.1002/mrm.26899.

[23] R. A. Rakow-Penner, N. S. White, D. J. Margolis, J. K. Parsons, N. Schenker-Ahmed, J. M. Kuperman, et al., "Prostate diffusion imaging with distortion correction," *Magn. Reson. Imaging.,* vol. 35, no. 9, pp. 1178-1181, Nov. 2015, doi: 10.1016/j.mri.2015.07.006.

[24] I. Hancu, S.-K. Lee, R. Lenkinski, D. Holland, J. I. Sperl and E. T. Tan, "Distortion correction in diffusion-weighted imaging of the breast: Performance assessment of prospective, retrospective, and combined (prospective + retrospective) approaches," *Magn. Reson. Med.,* vol. 78, no. 1, pp. 247-253, Jul. 2017, doi: 10.1002/mrm.26328.

[25] N. M. deSouza, M. Orton, K. Downey, V. A. Morgan, D. J. Collins, S. L. Giles, et al.,"Distortion correction of echo-planar diffusion-weighted images of uterine cervix," *J. Magn. Reson. Imaging.,* vol. 43, no. 5, pp. 1218-1223, May. 2016, doi: 10.1002/jmri.25080.

[26] J. Ceranka, M. Polfliet, F. Lecouvet, N. Michoux, J. de Mey and J. Vandemeulebroucke, "Registration strategies for multi-modal whole-body MRI mosaicing," *Magn. Reson. Med.,* vol. 79, no. 3, pp. 1684-1695, Jun. 2017, doi: 10.1002/mrm.26787.

[27] F. Jäger and J. Hornegger, "Nonrigid registration of joint histograms for intensity standardization in magnetic resonance imaging," *IEEE Trans. Med. Imaging,* vol. 28, no. 1, pp. 137-150, Jan. 2009, doi: 10.1109/TMI.2008.2004429.

[28] O. Dzyubachyk, M. Staring, M. Reijnierse, B. P. Lelieveldt and R. J. van der Geest, "Inter-station intensity standardization for whole-body MR data," *Magn. Reson. Med.,* vol. 77, no. 1, pp. 422-433, Feb. 2016, doi: 10.1002/mrm.26098.

[29] L. A. Digma, C. H. Feng, C. C. Conlin, A. E. Rodríguez-Soto, A. Y. Zhong and T. S. Hussain, "Correcting B0 inhomogeneity-induced distortions in whole-body diffusion MRI of bone," *Scientific Reports*, vol. 12, no. 1, Jan. 2022, Art. no. 265, doi: 10.1038/s41598-021-04467-2.

[30] UZ Leuven, *Protocol for an interventional study*, Leuven: UZ Leuven, 2024.

[31] J. Delpiano. *Fast mutual information of two images or signals.* (2024). MATLAB Central File Exchange. [Online]. Available: https://www.mathworks.com/matlabcentral/fileexchange/13289-fast-mutual-information-of-two-images-or-signals

[32] T. M. Cover and J. A. Thomas, "Entropy, Relative Entropy, and Mutual Information," in *Elements of Information Theory*, 2nd ed. New Jersey, John Wiley & Sons Inc., 2006, ch. 2, pp. 13-57.

[33] M. W. Haskell, J.-F. Nielsen and D. C. Noll, "Off-resonance artifact correction for MRI: A review," *NMR in biomedicine*, vol. 36, no. 5, Apr. 2023, doi: 10.1002/nbm.4867.

[34] W. Chen, A. D. Hoffman, H. Liu and X. Liu, "Organotropism: new insights into molecular mechanisms of breast cancer metastasis," *NPJ Precis Oncol.* , vol. 2, no. 4, pp. 1-12, Feb. 2018, doi: 10.1038/s41698-018-0047-0.

[35] K. N. Weilbaecher, T. A. Guise and L. K. McCauley, "Cancer to bone: a fatal attraction," *Nature Reviews Cancer*, vol. 11, pp. 411-425, Jun. 2011, doi: 10.1038/nrc3055.